CHANDRA OBSERVATIONS OF 3C RADIO SOURCES WITH z < 0.3: NUCLEI, DIFFUSE EMISSION, JETS, AND HOTSPOTS

Article (Published Version)

The Astrophysical Journal, 714:589–604, 2010 May 1 doi:10.1088/0004-637X/714/1/589

CHANDRA OBSERVATIONS OF 3C RADIO SOURCES WITH $z < 0.3$: NUCLEI, DIFFUSE EMISSION, JETS, AND HOTSPOTS

F. Massaro[1], D. E. Harris[1], G. R. Tremblay[2], D. Axon[2,3], S. A. Baum[4], A. Capetti[5], M. Chiaberge[6,7], R. Gilli[8], G. Giovannini[7,9], P. Grandi[10], F. D. Macchetto[6], C. P. O'Dea[2], G. Risaliti[11], and W. Sparks[6]

[1] Harvard-Smithsonian Astrophysical Observatory, 60 Garden Street, Cambridge, MA 02138, USA
[2] Department of Physics, Rochester Institute of Technology, Carlson Center for Imaging Science 76-3144, 84 Lomb Memorial Dr., Rochester, NY 14623, USA
[3] School of Mathematical & Physical Sciences, University of Sussex, Falmer, Brighton, BN2 9BH, UK
[4] Carlson Center for Imaging Science 76-3144, 84 Lomb Memorial Dr., Rochester, NY 14623, USA
[5] INAF-Osservatorio Astronomico di Torino, Strada Osservatorio 20, I-10025 Pino Torinese, Italy
[6] Space Telescope Science Institute, 3700 San Martin Drive, Baltimore, MD 21218, USA
[7] INAF-Istituto di Radioastronomia di Bologna, via Gobetti 101, 40129 Bologna, Italy
[8] INAF-Osservatorio Astronomico di Bologna, Via Ranzani 1, 40127 Bologna, Italy
[9] Dipartimento di Astronomia, Universita' di Bologna, via Ranzani 1, 40127 Bologna, Italy
[10] INAF–IASF-Istituto di Astrofisica Spaziale e fisica cosmica di Bologna, Via P. Gobetti 101, 40129 Bologna, Italy
[11] INAF-Osservatorio Astronomico di Arcetri, Largo E. Fermi 5, 50125 Firenze, Italy
Received 2009 December 18; accepted 2010 March 4; published 2010 April 13

ABSTRACT

We report on our *Chandra* Cycle 9 program to observe half of the 60 (unobserved by *Chandra*) 3C radio sources at $z < 0.3$ for 8 ks each. Here we give the basic data: the X-ray intensity of the nuclei and any features associated with radio structures such as hotspots and knots in jets. We have measured fluxes in soft, medium, and hard bands and are thus able to isolate sources with significant intrinsic column density. For the stronger nuclei, we have applied the standard spectral analysis which provides the best-fit values of X-ray spectral index and column density. We find evidence for intrinsic absorption exceeding a column density of 10^{22} cm^{-2} for one-third of our sources.

Key words: galaxies: active – radio continuum: galaxies – X-rays: general

Online-only material: color figures

1. INTRODUCTION

Extended radio galaxies are classified into two main types (Fanaroff & Riley 1974; Miley 1980; Bridle & Perley 1984). The more powerful sources (Fanaroff–Riley class II, FR II) tend to have an edge-brightened radio structure dominated by compact bright hotspots. These sources often show either no or one jet which may be relativistic along its entire length (Laing 1988; Garrington et al. 1988). The lower luminosity sources (Fanaroff–Riley class I, FR I) tend to have edge-darkened structures which resemble "plumes" and usually exhibit two jets. The jets in FR Is may initially be launched relativistically but seem to decelerate on sub-kiloparsec scales likely through interaction with the environment (e.g., Laing et al. 2008). There are intrinsic differences in the central active galactic nucleus (AGN) of these two types of sources (e.g., Baum et al. 1995; Evans et al. 2006; Hardcastle et al. 2009). Most narrow-line FR IIs and a few FR Is show evidence for a hidden quasar continuum source and broad-line region (BLR; e.g., Cohen et al. 1999; Tadhunter et al. 2007). The sources with the hidden quasar also produce optical emission line nebulae with high ionization lines (High Excitation Galaxies, HEGs), while those without the hidden quasar produce only low ionization lines (Low Excitation Galaxies, LEGs; e.g., Hine & Longair 1979; Laing et al. 1994; Rector & Stocke 2001). There are also radio sources with properties intermediate between the FR Is and FR IIs, e.g., the "Fat Doubles" (Owen & Laing 1989).

The two main unsolved issues concern the origin of the FR I/FR II dichotomy (how it is related to different acceleration and emission processes), and the nature of the different emission-line regions between LEGs and HEGs (see Chiaberge et al. 2002; Hardcastle et al. 2007).

The morphological features of extragalactic radio sources can be described naturally with a small number of components: core, jets, hotspots, and lobes. While their radio to optical emission is typically described in terms of synchrotron radiation by relativistic particles, the origin of X-ray emission in extended structures (jets and hotspots) is still unclear, but certainly non-thermal (Harris & Krawczynski 2002). The main open question lies in which mechanism, synchrotron or inverse Compton (IC) scattering, dominates the X-ray emission. The former describes emission from low-power jets (Harris & Krawczynski 2006), while the latter provides a good explanation for high-power radio galaxy and quasar jets, in which the seed photons for the IC scattering could be the cosmic microwave background (CMB; Tavecchio et al. 2000).

Only by combining X-ray observations with historical and/or simultaneous data in other wavebands is it possible to build up the spectral energy distribution (SED) of cores, jets, and hotspots and to compare them with synchrotron or IC models to investigate the origin of their emission.

During the last few years, several snapshot surveys of 3C radio galaxies have been carried out using the *Hubble Space Telescope* (*HST*) in red, blue, ultraviolet and near-IR continuum, and optical spectroscopy which approaches the statistical completeness of the radio catalog: ∼90%. A ground-based spectroscopic program for the whole sample with the Galileo Telescope has been completed (Buttiglione et al. 2009). We also obtained deep ground-based IR *K*-band imaging.

Radio images with arcsec resolution are available for most 3C sources from colleagues, the National Radio Astronomy Observatory (NRAO) Very Large Array (VLA) Archive Survey (NVAS), and the archives of the VLA and MERLIN. Very Long Baseline Array (VLBA) data for some 3C objects with $z < 0.2$

Table 1
Source List of the *Chandra* AO9 Snapshot Survey of 3C Radio Sources with $z < 0.3$

3C	Class[a]	R.A. (J2000) hh mm ss	Decl. (J2000) dd mm ss	z[b]	D_L (Mpc)	Scale (kpc arcsec^{-1},)	N_H[c] (cm^{-2})	m_v[d]	S_{178}[e] (Jy)	*Chandra* Obs ID	Obs. Date (yyyy-mm-dd)
17	?–BLO	00 38 20.528	−02 07 40.49	0.2197	1078.8	3.516	2.86e20	18.0	20.0	9292	2008-02-02
18	FR II–BLO	00 40 50.553	+10 03 26.78	0.188	905.7	3.111	5.33e20	18.5	19.0	9293	2008-06-01
20	FR II–HEG	00 43 09.177	+52 03 36.05	0.174	831.0	2.923	1.84e21	19.0	42.9	9294	2007-12-31
33.1	FR II–BLO	01 09 44.237	+73 11 57.10	0.181	868.2	3.018	2.00e21	19.5	13.0	9295	2008-04-01
52	FR II (X)	01 48 28.909	+53 32 28.04	0.2854	1454.5	4.268	1.67e21	18.5	13.5	9296	2008-03-26
61.1	FR II–HEG	02 22 35.571	+86 19 06.38	0.1878	904.6	3.108	7.87e20	19.0	31.2	9297	2008-12-05
76.1	FR I	03 03 15.054	+16 26 18.83	0.0324	140.3	0.638	9.49e20	14.9	12.2	9298	2007-12-09
105	FR II–HEG	04 07 16.453	+03 42 25.80	0.089	401.7	1.642	1.15e21	18.5	17.8	9299	2007-12-17
132	FR II–LEG	04 56 42.919	+22 49 23.20	0.214	1047.3	3.445	2.11e21	18.5	13.7	9329	2008-03-26
133	FR II–HEG	05 02 58.472	+25 16 25.31	0.2775	1408.2	4.183	2.54e21	20.0	22.3	9300	2008-04-07
135	FR II–HEG	05 14 08.367	+00 56 32.28	0.1273	589.9	2.250	8.73e20	17.1	17.3	9301	2008-01-10
153	FR II–LEG	06 09 32.423	+48 04 14.64	0.2769	1404.7	4.177	1.65e21	18.5	15.3	9302	2007-12-07
165	FR II–LEG	06 43 07.400	+23 19 03.00	0.2957	1481.6	4.317	1.93e21	19.5	13.5	9303	2008-02-02
171	FR II–HEG	06 55 14.722	+54 08 57.46	0.2384	1183.5	3.741	5.65e20	18.9	19.5	9304	2007-12-22
184.1	FR II–BLO	07 43 01.394	+80 26 26.09	0.1182	544.4	2.111	3.15e20	17.0	13.0	9305	2008-03-27
197.1	FR II–BLO	08 21 33.605	+47 02 37.40	0.1301	604.0	2.293	4.20e20	16.5	8.1	9306	2007-12-16
213.1	FR II–LEG (CSS)	09 01 05.269	+29 01 46.88	0.1937	936.4	3.186	2.45e20	19.0	6.6	9307	2008-04-14
223.1	FR II–HEG (X)	09 41 24.019	+39 44 41.62	0.1075	491.5	1.943	1.31e20	16.4	6.0	9308	2008-01-16
287.1	FR II–BLO	13 32 53.257	+02 00 45.60	0.2156	1056.1	3.465	1.63e20	18.3	8.2	9309	2008-03-23
293	FR I–LEG	13 52 17.789	+31 26 46.44	0.045	196.7	0.873	1.27e20	14.4	12.7	9310	2008-03-19
300	FR II–HEG	14 22 59.861	+19 35 36.72	0.27	1364.5	4.101	2.49e20	18.0	17.9	9311	2008-03-21
303.1	FR II–HEG (CSS)	14 43 14.800	+77 07 29.00	0.267	1347.1	4.068	3.16e20	19.0	8.1	9312	2008-02-21
305	FR I–HEG (CSS)	14 49 21.661	+63 16 14.12	0.0416	181.4	0.811	1.31e20	13.7	15.7	9330	2008-04-07
315	FR I–LEG (X)	15 13 40.054	+26 07 30.06	0.1083	495.4	1.955	4.27e20	16.3	17.8	9313	2007-12-10
323.1	Quasar–BLO	15 47 43.545	+20 52 16.54	0.2643	1331.4	4.038	3.79e20	16.7	9.7	9314	2008-06-01
332	FR II–BLO	16 17 42.540	+32 22 34.49	0.1515	713.2	2.608	1.79e20	16.0	9.6	9315	2007-12-10
349	FR II–HEG	16 59 28.893	+47 02 55.04	0.205	997.8	3.332	1.88e20	19.0	13.3	9316	2008-12-28
381	FR II–HEG	18 33 46.301	+47 27 02.61	0.1605	760.0	2.736	6.15e20	17.5	16.6	9317	2008-02-21
436	FR II–HEG	21 44 11.743	+28 10 18.91	0.2145	1050.0	3.451	6.42e20	18.2	17.8	9318	2008-01-08
460	FR II–LEG	23 21 28.510	+23 46 48.45	0.268	1352.9	4.079	4.72e20	18.8	8.2	9319	2008-06-04

Notes.
[a] The "class" column contains both a radio descriptor (Fanaroff-Riley class I or II) and a spectroscopic designation: LEG, "Low Excitation Galaxy," HEG, "High Excitation Galaxy," and BLO, "Broad-Line Object"; Buttiglione et al. 2009). "CSS" designates "Compact Steep Spectrum" (a radio term), while "X" is used for "X-shaped" radio morphology.
[b] Redshift estimates are taken from Chiaberge et al. (2002), Floyd et al. (2006), and Buttiglione et al. (2009).
[c] Neutral hydrogen column densities are taken from Kalberla et al. (2005).
[d] m_v is the visual magnitude (Spinrad et al. 1985).
[e] S_{178} is the flux density at 178 MHz, taken from Spinrad et al. (1985).

have already been obtained (see, e.g., Giovannini et al. 2001, Liuzzo et al. 2009, and references therein).

Chandra is the only X-ray facility that can offer angular resolution comparable to the optical and radio. Previous X-ray studies are mostly biased toward observations of a special group of X-ray bright sources or objects with well known interesting features or peculiarities instead of carefully selected samples, unbiased with respect to orientation and spectroscopic classification.

The general goals of our program are to discover new jets and hotspots, determine their emission processes on a firm statistical basis, study the nuclear emission of the host galaxy, and derive SEDs for an unbiased sample of objects. The resulting data set will be used to test the unification model and study the nature of nuclear absorption.

This paper consists of all the basic data for this *Chandra* sample. After a description of the observations and data reduction (Section 2), we give the general and particular results in Section 3. Section 4 contains a short summary.

For our numerical results, we use cgs units unless stated otherwise and we assume a flat cosmology with $H_0 = 72$ km s^{-1} Mpc^{-1}, $\Omega_M = 0.27$, and $\Omega_\Lambda = 0.73$ (Spergel et al. 2007). Spectral indices, α, are defined by flux density, $S_\nu \propto \nu^{-\alpha}$.

2. OBSERVATIONS AND DATA REDUCTION

The sources observed in this project are listed in Table 1 together with their salient parameters. Each was observed for a nominal 8 ks, and the actual live times are given in Table 2, together with the nuclear fluxes. We used the ACIS-S very faint mode with standard readout times (3.2 s). The 15 observations made through 2008 February had five chips turned on: I2, I3, S1, S2, and S3. When we analyzed the data from 3C 436 taken on 2008 January 10, we found a background around twice nominal on the two back-illuminated chips. This had the unfortunate consequence of producing a total count rate essentially equal to the telemetry saturation of 68.8 counts s^{-1}. Therefore, to minimize the chances of this occurring again, all observations made after 2008 March 1 had the back-illuminated chip S1 turned off. Ex post facto, we checked the evt1 count rate for the 14 other observations made with the five chips on. These ranged from 43 to 61 counts s^{-1}, safely below the telemetry limit.

Table 2
Nuclear X-ray Fluxes in Units of 10^{-15} erg cm^{-2} s^{-1}

3C	LivTim[a] (ks)	Net[b] (counts)	Ext. Ratio[c]	f (soft) 0.5–1 keV	f (medium) 1–2 keV	f (hard) 2–7 keV	f (total) 0.5–7 keV	$\frac{\text{HARD}}{\text{MEDIUM}}$[d]	N_H[e] (10^{22} cm^{-2})	L_X (10^{42} erg s^{-1})
17*	7.93	1151 (34)	0.98 (0.04)	139 (9)	193 (9)	695 (34)	1030 (37)	3.6 (0.2)	···	143 (5)
18*	7.94	1045 (32)	0.88 (0.04)	86.9 (6.9)	149 (8)	909 (40)	1140 (41)	6.1 (0.4)	1.4 (0.6)	112 (4)
20	7.93	147 (12)	0.93 (0.12)	···	1.36 (0.78)	286 (24)	287 (24)	210 (121)	10.2 (0.7)	23.7 (2.0)
33.1	8.07	692 (26)	0.95 (0.05)	3.5 (1.4)	40.0 (4.3)	1080 (44)	1120 (45)	27 (3)	4.7 (0.7)	101 (4)
52	8.02	11 (3)	0.85 (0.60)	···	1.13 (0.65)	14.5 (5.5)	15.6 (5.6)	12.8 (8.8)	3.0 (2.0)	4.0 (1.4)
61.1	8.05	51 (7)	0.99 (0.26)	1.61 (0.93)	5.9 (1.6)	66 (12)	74 (11)	11 (3)	2.6 (0.7)	7.2 (1.1)
76.1	8.06	27 (5)	0.64 (0.20)	···	3.1 (1.3)	26.2 (6.6)	29.3 (6.7)	8 (4)	1.9 (1.3)	0.069 (0.016)
105	8.07	308 (18)	0.93 (0.08)	3.0 (2.2)	6.3 (1.6)	699 (41)	708 (42)	111 (28)	8.5 (0.7)	13.7 (0.8)
132	7.69	42 (6)	1.00 (0.28)	···	2.3 (1.2)	69 (11)	69 (11)	30 (16)	5.0 (0.6)	9.1 (1.5)
133	8.03	623 (25)	0.99 (0.06)	22.7 (3.5)	138 (7.7)	412 (26)	573 (27)	3.0 (1.9)	···	136 (6)
135	7.93	40 (6)	0.82 (0.21)	3.7 (1.5)	5.0 (1.4)	45 (10)	54 (10)	9 (3)	2.16 (1.19)	2.26 (0.43)
153	8.06	···	···	···	···	···	···	···	···	···
165	7.67	35 (6)	0.41 (0.10)	···	5.2 (1.5)	43.6 (9.1)	48.8 (9.2)	8 (3)	1.9 (1.3)	12.8 (2.4)
171	7.93	184 (14)	0.69 (0.07)	1.7 (1.0)	5.6 (1.5)	312 (24)	319 (24)	55 (16)	6.5 (0.7)	53.5 (4.1)
184.1	8.02	535 (23)	0.94 (0.06)	6.6 (1.8)	25.6 (3.4)	864 (40)	896 (41)	34 (4)	5.2 (0.7)	31.8 (1.4)
197.1	7.96	860 (29)	0.95 (0.05)	103 (8)	157 (8)	541 (31)	801 (33)	3.4 (0.3)	···	35.0 (1.4)
213.1	8.07	65 (8)	0.56 (0.10)	9.5 (2.2)	13.6 (2.3)	21.2 (6.1)	44.3 (6.9)	1.6 (0.5)	···	4.65 (0.72)
223.1	7.93	178 (13)	0.90 (0.10)	8.6 (2.1)	4.1 (1.3)	313 (32)	326 (32)	76 (25)	7.4 (0.7)	9.42 (0.92)
287.1*	8.02	1095 (33)	0.90 (0.04)	117 (8)	169 (8)	763 (39)	1050 (40)	4.5 (0.3)	···	140 (5)
293	7.81	215 (15)	0.69 (0.07)	4.0 (1.5)	6.6 (1.7)	381 (28)	392 (29)	58 (15)	6.7 (0.7)	1.81 (0.13)
300	7.94	162 (13)	0.92 (0.11)	23.6 (3.5)	30.7 (3.6)	67 (10)	122 (11)	2.2 (0.4)	···	27.2 (2.5)
303.1	7.67	19 (4)	0.41 (0.13)	3.7 (1.4)	1.87 (0.93)	9.9 (4.4)	15.8 (4.7)	5 (4)	···	3.4 (1.0)
305	8.22	63 (8)	0.31 (0.04)	12.0 (2.5)	10.4 (2.0)	13.8 (4.9)	36.2 (5.9)	1.3 (0.5)	···	0.143 (0.023)
315	7.67	6 (2)	0.50 (0.36)	···	···	9.6 (4.8)	9.6 (4.8)	···	···	0.28 (0.14)
323.1*	7.93	512 (23)	0.70 (0.04)	31.6 (3.9)	62.7 (6.3)	532 (35)	626 (36)	8 (1)	1.9 (0.8)	133 (8)
332*	7.93	736 (27)	0.80 (0.04)	29.3 (3.9)	82.7 (6.1)	931 (43)	1040 (43)	11 (1)	2.6 (0.7)	63.3 (2.6)
349	8.02	230 (15)	0.97 (0.10)	5.4 (1.7)	40.0 (4.2)	212 (19)	257 (19)	5.3 (0.7)	···	30.6 (2.3)
381	8.06	246 (16)	0.96 (0.10)	10.3 (2.2)	9.4 (2.0)	415 (29)	435 (30)	44 (10)	5.9 (0.5)	30.1 (2.0)
436	8.04	43 (7)	0.27 (0.06)	2.4 (1.2)	2.25 (0.92)	68 (12)	72 (12)	30 (13)	5.0 (0.6)	9.5 (1.6)
460	8.05	44 (7)	0.88 (0.20)	4.9 (1.6)	3.2 (1.2)	50.4 (9.7)	58.5 (9.9)	16 (7)	3.4 (0.5)	12.8 (2.2)

Notes. Values in parentheses are 1σ uncertainties. An "*" indicates the source was adversely affected by pileup. See the note added in proof.
[a] LivTim is the live time.
[b] Net is the net counts within a circle of radius $= 2''$.
[c] Ext. Ratio ("Extent Ratio") is the ratio of the net counts in the $r = 2''$ circle to the net counts in the $r = 10''$ circle. Values significantly less than 0.9 indicate the presence of extended emission around the nuclear component.
[d] In the absence of absorption, the ratio of hard flux to medium flux should lie in the range 0.5–5 for "normal" power laws (see the text). Thus, values significantly larger than 6 indicate substantial intrinsic absorption.
[e] As per the discussion in the text, we calculate the value of N_H required to produce the observed ratio of hard/medium flux. The uncertainty given here is indicative only: it is the range of N_H covered by the uncertainty in the ratio and allowing α_x to range from 0.5 to 1.0. Obviously there may be some sources with intrinsic spectral indices outside of this range.

The data reduction has been performed following the standard reduction procedure described in the *Chandra* Interactive Analysis of Observations (CIAO) threads,[12] using CIAO version 3.4 and the *Chandra* Calibration Database (CALDB) version 3.4.2. Level 2 event files were generated using the *acis_process_events* task, after removing the hot pixels with *acis_run_hotpix*. Events were filtered for grades 0, 2, 3, 4, 6, and we removed pixel randomization.

Light curves for every data set were extracted and checked for high-background intervals; none was found except for 3C 436 which was contaminated by a very high background during the entire exposure so that time filtering was not an option.

Astrometric registration was achieved by changing the appropriate keywords in the fits header so as to align the nuclear X-ray position with that of the radio. We also registered the *HST* images in the same way.

[12] http://cxc.harvard.edu/ciao/guides/index.html

2.1. Flux maps

We created three different flux maps (soft, medium, and hard in the ranges 0.5–1, 1–2, and 2–7 keV, respectively) by dividing the data with monochromatic exposure maps (with nominal energies of soft = 0.8 keV, medium = 1.4 keV, and hard = 4 keV). The exposure maps and the flux maps were regridded to a common pixel size which was usually 1/4 the size of a native ACIS pixel (native = 0.″492). For sources of large angular extent, we used 1/2 or no regridding. To obtain maps with brightness units of erg cm^{-2} s^{-1} pixel^{-1}, we multiplied each event by the nominal energy of its respective band.

To measure observed fluxes for each feature, we construct an appropriate region (usually circular) and two adjacent background regions of the same size. The two background regions were chosen so as to avoid contaminating X-ray emission (and also radio emission) and permitted us to sample both sides of jet features, two areas close to hotspots, and avoid contamination from weak emission surrounding the nuclei of the galaxies.

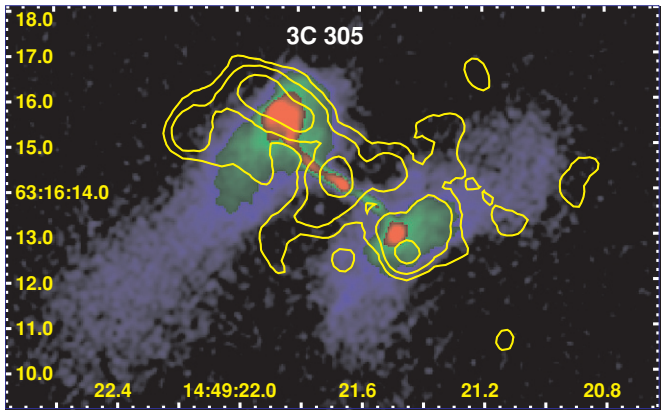

Figure 1. 3C 305, an example of a CSS source. The radio image is from a 1.5 GHz observation (see Massaro et al. 2009a, and references therein). The X-ray contours come from our 0.5–7 keV image, rebinned to 0.″123 pixels, and smoothed with a Gaussian of FWHM = 0.″72. The lowest contour is 0.04 counts per pixel and successive contours increase by factors of 2.

(A color version of this figure is available in the online journal.)

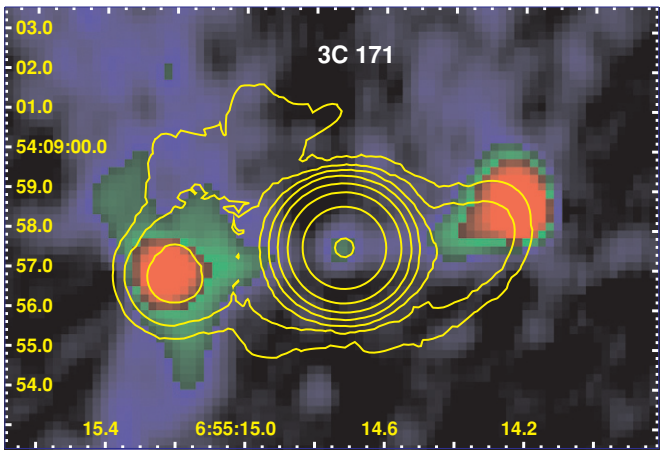

Figure 2. 3C 171, a small FR II radio galaxy with extended emission surrounding the nucleus. The radio image comes from an 8 GHz VLA observation (Hardcastle 2003). The X-ray contours come from an image rebinned as in Figure 1, smoothed with a Gaussian of FWHM = 1.″9. The lowest contour is at 0.005 counts per pixel and contours increase by factors of 2. (Radio map kindly supplied by M. Hardcastle.)

(A color version of this figure is available in the online journal.)

We then measure the net flux in each region and in each energy band with funtools.[13] Measured fluxes were corrected by the ratio of the mean energy within the photometric aperture to the nominal energy. This correction ranged from a few to 15%. A 1σ error is assigned based on the usual $\sqrt{\text{number of counts}}$ in the on and background regions.

2.2. Spectral Analysis of the Stronger Nuclei

2.2.1. Extraction of Point-source Nuclear Spectra

We have performed a "first-pass" nuclear point-source spectral analysis for those sources with greater than 50 counts in a 2″ aperture centered around the nucleus (see Column 3 of Table 2). Sources with fainter nuclei were excluded from our analysis as sufficient signal and resolution in energy space is required for robust constraints on multi-parameter model fits. The unresolved nuclear spectra were extracted using the CIAO routine `psextract`, wherein sources with greater than 300 counts in the 2″ aperture were binned to 30 counts while fainter sources were not binned. Binned spectra were fit using χ^2 statistics, while unbinned spectra were fit using Cash statistics (Cash 1979).

2.2.2. Model Fits

We have fit a three-component absorbed power-law model to each extracted spectrum using the NASA HEASARC software package XSPEC (Arnaud 1996). The multiplicative model used (in XSPEC syntax) is `wabs`×`zwabs`×`zpowerlw`, and consists of a galactic photoelectric neutral hydrogen absorption component (`wabs`), a redshifted "intrinsic" neutral absorption component (`zwabs`), and a redshifted power law (`zpowerlw`). The power law itself is defined by the target redshift, the photon index, and a normalization scale factor. For each fit the Milky Way absorption (`wabs`) was fixed (see Column 3 of Table 4), alongside the target redshift (a parameter in both `zwabs` and `zpowerlw`). The three remaining "thawed" parameters, consisting of the intrinsic absorption (hereafter $N_H\,(z)$), photon index, and normalization, were allowed to vary in the "first-pass" fit.

As stated previously, Gaussian (χ^2) statistics were used in fitting binned (to 30 counts) spectra with greater than 300 counts (i.e., yielding at least 10 binned channels in unfiltered energy space) and Cash statistics were used for the fainter unbinned spectra. The spectra for 3C 105 and 3C 381 were binned to 15 counts, as 30 count bins sacrificed too much resolution in energy space, resulting in poor fits. All the fitting procedures have been performed in the 0.3–8.0 keV energy range.

In general, these first-pass fits with three variable parameters were unsuccessful in constraining both the photon index and the intrinsic column density to within a reasonable confidence interval. An overriding issue is that, for ostensibly "heavily absorbed sources" (judging from hard-to-med band flux ratios), one is limited by steep absorption falloff at the soft end and by declining effective area on the hard end, effectively limiting the spectral fit to less than one decade in energy space. The first-pass XSPEC fits required fitting the absorption component and photon index using the same region of the spectrum, such that typically XSPEC would be successful in fitting one but yield unphysical or unconstrained values for the other parameter. All the results of the spectral analysis are summarized in Table 4.

3. RESULTS

3.1. General

X-ray emission was detected for all the nuclei in the sample except for 3C 153, a small size FR II radio galaxy with a radio-quiet (<0.5 mJy beam^{-1}) core (see Laing 1981; Figure 19). The observed nuclear fluxes are presented in Table 2 in the soft, medium, and hard bands together with the X-ray luminosity. The number of counts and the ratio of net counts ($r = 2''$ divided by $r = 10''$) are also given. This ratio should be close to unity for an unresolved source: the on-axis encircled energy for $r = 2''$ is ≈0.97, so we expect only a small increase between $r = 2''$ and $r = 10''$ for an unresolved source.

Amongst the detected sources are three compact steep spectrum (CSS) radio sources: 3C 213.1, 3C 303.1, and 3C 305 (see Figure 1). A detailed analysis of 3C 305 has already been published (Massaro et al. 2009a). We also found a radio source with soft X-ray emission presumably associated with thermal gas of the host galaxy, 3C 171 (see Figure 2). For six of our sources, we have detections of a hotspot with confidence levels between

[13] http://www.cfa.harvard.edu/~john/funtools

Table 3
Radio Hotspots with X-ray Detections

3C	Hotspot[a]	Radius[b] (arcsec)	Counts (bkg)[c]	$f_{0.5-1\ keV}$ (cgs)	$f_{1-2\ keV}$ (cgs)	$f_{2-7\ keV}$ (cgs)	$f_{0.5-7\ keV}$ (cgs)	L_X (10^{41} erg s^{-1})
52	N 34	1.2	5 (0.45)	1.21 (0.85)	1.27 (0.75)	...	2.5 (1.1)	6.3 (2.9)
61.1	S 102	4.0	9 (5.2)	1.56 (0.90)	1.08 (0.78)	4.8 (2.8)	7.5 (4.5)	7.3 (4.3)
105	S 166	1.5	14 (1.1)	2.3 (1.1)	1.74 (0.87)	9.7 (4.0)	13.7 (4.2)	2.65 (0.82)
	S 169	1.5	5 (1.1)	0.46 (0.46)	0.52 (0.52)	4.8 (2.8)	5.8 (2.9)	1.11 (0.55)
213.1	N 4	1.0	3 (0.40)	...	0.70 (0.50)	0.63 (0.17)	1.3 (0.5)	1.40 (0.54)
287.1	W 65	5.0	10 (7.7)	2.3 (1.2)	1.30 (0.90)	4.5 (3.2)	8.1 (3.5)	10.8 (4.6)
349	S 38	2.0	4 (0.70)	0.51 (0.51)	0.67 (0.47)	1.5 (1.5)	2.7 (1.6)	3.17 (2.0)
	S 43	2.0	6 (0.70)	0.40 (0.40)	1.55 (0.77)	0.98 (0.98)	2.9 (1.3)	3.48 (1.56)

Notes. Fluxes are given in units of 10^{-15} erg cm^{-2} s^{-1}.
[a] The hotspot designation is comprised of a cardinal direction plus the distance from the nucleus is arcsec.
[b] The radius column gives the size of the aperture used for photometry.
[c] The counts column gives the total counts in the photometric circle together with the expected background counts in parentheses; both for the 0.5–7 keV band.

Table 4
Best-fit Parameters from Spectral Analysis

Source	Bin Size (counts)	Galactic N_H ($\times 10^{22}$ cm^{-2})	Intrinsic N_H (z) ($\times 10^{22}$ cm^{-2})	α_x	Red. χ^2	Cstat/dof (dof)
(1)	(2)	(3)	(4)	(5)	(6)	(7)
3C 17*	30	0.0286	<0.05	0.3 (0.1)	0.81	0.664 (333)
3C 18*	30	0.0533	<0.09	−0.16 (0.12)	1.50	0.853 (342)
3C 20	1	0.1840	13 (6)	0.5 (1.1)	...	0.802 (113)
3C 33.1	30	0.2000	4 (2)	0.2 (0.5)	1.19	0.862 (316)
3C 61.1	1	0.0787	<0.04	1.0 (0.15)	...	0.989 (187)
3C 105	15	0.1150	31 (20)	0.20	1.32	1.091(180)
3C 133	30	0.2540	1.0 (0.4)	1.15 (0.3)	1.99	1.017(236)
3C 171	1	0.0565	6 (0.3)	0.20 (0.7)	...	0.853(144)
3C 184.1	30	0.0351	4.0 (1.3)	−0.13 (0.5)	1.09	0.857 (295)
3C 197.1	30	0.0420	<0.1	0.4 (0.2)	1.30	0.911 (281)
3C 223.1	1	0.0131	25 (15)	0.98	...	1.306 (131)
3C 287.1*	30	0.0163	<0.03	0.04 (0.1)	1.08	0.815 (328)
3C 293	1	0.0127	...	...	...	...
3C 300	1	0.0249	<0.2	0.6 (0.4)	...	0.816 (106)
3C 305	1	0.0131	...	...	...	...
3C 323.1*	30	0.0379	<0.2	−0.6 (0.2)	1.18	0.874 (282)
3C 332*	30	0.0179	...	...	...	...
3C 349	1	0.0188	0.9 (0.4)	0.2 (0.4)	...	...
3C 381	15	0.0615	27 (3)	1.0	0.802	1.079 (178)

Notes. An "*" indicates the source was adversely affected by pileup. See the note added in proof. Summary of results of our spectral analysis for the brighter nuclei in our sample (those sources with greater than 50 counts in a 2″ nuclear aperture). (1) 3C source name; (2) bin size, in counts, of the point-source spectrum extracted from the 2″ aperture centered about the nucleus. Those sources whose spectra have been binned to 30 (or in a few cases 15), counts were analyzed in XSPEC using χ^2 statistics. Unbinned spectra (listed as binned to 1 count in Column 2) were analyzed using Cash statistics (Cash 1979). Note that all binned (30 counts) spectra were also analyzed with Cash to check for consistency in parameter fits and model flux values. The result of this analysis showed reasonable consistency between the two statistics models, though a goodness-of-fit indicator was lacking for Cash statistics. (3) Fixed galactic absorbing neutral hydrogen column density (Kalberla et al. 2005). (4) Best-fit redshifted neutral hydrogen absorption component. Those sources listed with no entries have an unconstrained N_H (z), owing to (a) low intrinsic absorption and/or (b) degeneracy in the model fit. (5) Best-fit spectral index; (6) Reduced χ^2 of the given fit, listed only for binned spectra. A goodness-of-fit indicator is not available for the unbinned spectra as Cash statistics were used in their model fits. (7) Cash statistic divided by dof. The dof values are given in parentheses.

1σ and 14σ. In 3C 105 (see Figure 3), we find two emission regions: one coincident with the radio hotspot itself and another which seems to be the jet entering into the hotspot region. Fluxes for these are reported in Table 3. Finally, we detected two knots in the curved jet of 3C 17 (see Figure 4); details have been published (Massaro et al. 2009b).

3.2. Incidence of Intrinsic Absorption

According to the unified scheme, since a large fraction of our current sample are FR II radio galaxies, we may expect some sources to show a significant amount of absorbing material along the line of sight to the nuclei of these galaxies. Indeed, we see evidence of high absorption both from the flux map data and the spectral analyses.

Most nuclei of AGN have X-ray spectra which are well described by power laws with α_x values ranging from 0.5 to 1.5 or occasionally larger. For those sources with little intrinsic absorbing material (i.e., the galactic N_H values are the major contributors to the total absorption), the expected ratio of hard to medium flux can be easily calculated based on the chosen energies defining the relevant bands. For our standard bands,

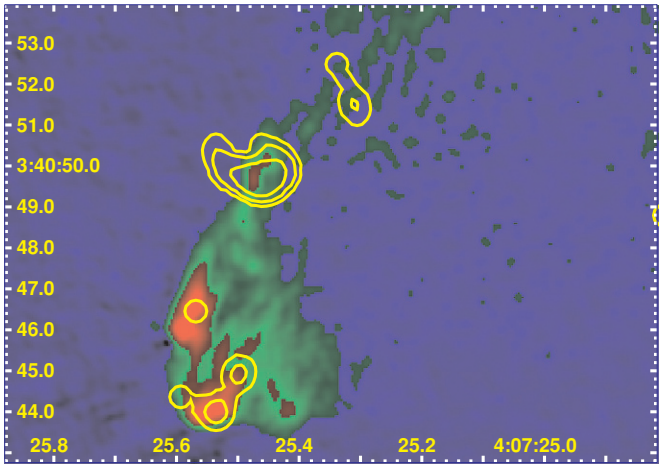

Figure 3. S hotspot of 3C 105. The image is from the VLA; an 8 GHz map with a beam of FWHM = 0.″25. The contours come from a *Chandra* flux map (0.5–7 keV) smoothed with a Gaussian of FWHM = 0.″7. The lowest contour is 0.02 counts per pixel and the pixel size is 0.″123. Subsequent contours increase by factors of 2. Note that the brighter X-ray emission coincides with a radio feature which could be described as the jet entering the hotspot region. X-ray emission is also detected from the (radio) brighter terminal hotspot. (Radio map kindly supplied by M. Hardcastle.)

(A color version of this figure is available in the online journal.)

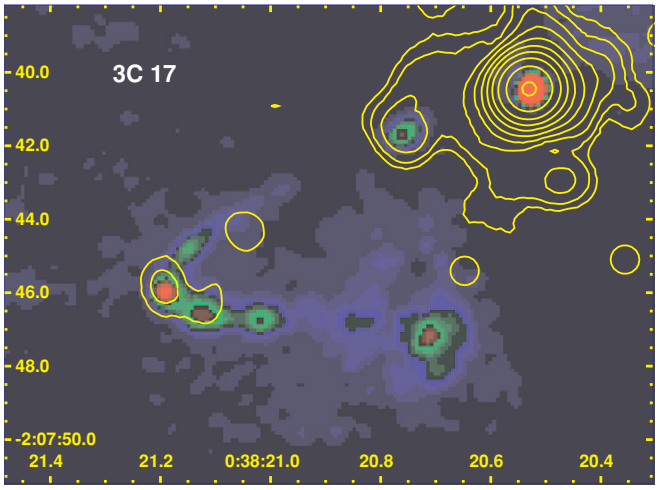

Figure 4. 3C 17 with a one-sided, curved jet. The radio image is that of Morganti et al. (1999) at 5 GHz. The X-ray contours come from our image with a smoothing function of 1″. The lowest contour is 0.02 counts per pixel (with pixel = 0.″123). (Radio map kindly supplied by R. Morganti.)

(A color version of this figure is available in the online journal.)

these ratios run from 1 to 3, depending of course on the actual value of α_x. Even for extreme values of α_x such as 0 or 2.5, the ratios are 5 and 0.5, respectively. In Table 2 we give the observed values of this ratio, together with the uncertainties derived from the errors on the flux values. About half of our sample have ratios that are larger than 6, even after allowing them to take on their minimum value (i.e., value minus error). We suspect that all of these have significant intrinsic absorption since, in the absence of such absorption, α_x would have to have a value less than zero.

A similar method to derive evidences of intrinsic absorption from the flux ratios in different energy ranges have been used by Alexander et al. (2001, 2002) for large sample of AGNs. However, if the sources are Compton thick (i.e., $N_H > 10^{24}$ cm^{-2}) or if the spectrum is inverted (i.e., $\alpha_x < 0$), the ratios will not provide a good estimate of absorption. In particular, for

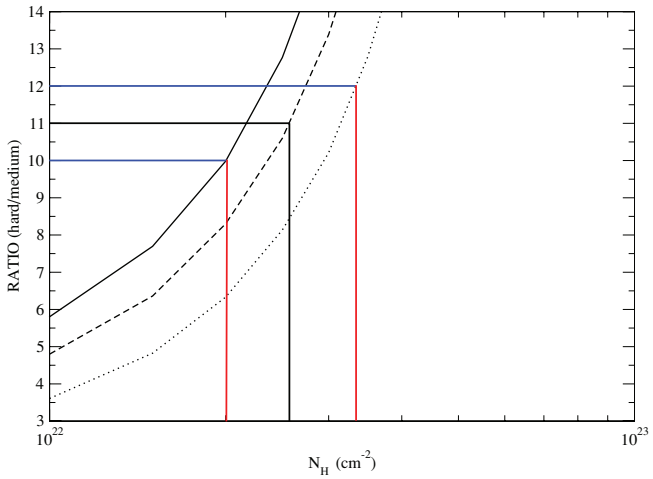

Figure 5. Results of simulating spectra for a range of intrinsic absorption and a range of α_x. The ratio of hard/medium flux is plotted on the vertical axis and the column densities are plotted along the x axis. The three curves (left to right) correspond to $\alpha_x = 0.5$, 0.7, and 1. The example shown is for 3C 332 which has a ratio of 11 ± 1.

(A color version of this figure is available in the online journal.)

Compton thick sources, even if they are very rare among radio-loud AGNs, the spectrum could be dominated by a reflection component providing a ratio of ∼5–10 indicating a low intrinsic absorption even if the source is heavily absorbed.

We note that the values of the neutral absorption estimated using the photometric method and evaluated from the spectral analysis could be different. This happens because the photometric method is based on the assumption that the intrinsic spectrum is a simple power law. If the spectrum has some features, as, for example, emission lines, the estimates of intrinsic N_H could be different, as in the case of 3C 105, and only the detailed spectral fitting procedure will provide the correct information.

Much the same conclusion can be reached by the difficulty of fitting a power law plus absorption to the brighter sources. The fact that XSPEC returns small values of α_x we ascribe to the situation of a heavily absorbed spectral distribution for which it is difficult to define the actual power law above 2 keV where the effective area of the instrument is falling. What we are dealing with is an inadequate segment of the spectrum which is essentially flat or inverted, around the peak in the SED.

Even though we may not be able to recover the parameters of interest (α_x and N_H) from the spectral fits, it is possible to demonstrate a range of intrinsic N_H column densities corresponding to some chosen range in α_x by using "fake" spectra in XSPEC. An example for 3C 332 is shown in Figure 5. Corresponding to the ratio of hard to medium flux of 11 ± 1, we find a range of $(2–3.2) \times 10^{22}$ cm^{-2} for α_x between 0.5 and 1. We have run these calculations (the "photometric method") for each source with large hardness ratio and thus suspected to have large intrinsic absorption. These results are given in Table 2. Comparing N_H values from XSPEC to those calculated from the ratio of hard/medium, we find reasonable agreement for five sources (3C 20, 33.1, 61.1, 171, and 184.1). For 3C 133, the photometric method gives a value five times larger than the spectral analysis, and for three sources (3C 105, 223.1, and 381) we find spectral values 3–5 times larger than their respective photometric values. Given the difficulties in spectral fitting (Section 2.2) together with the likely wider range in α_x than used in our calculations, we do not think it necessary to pursue these disparities further.

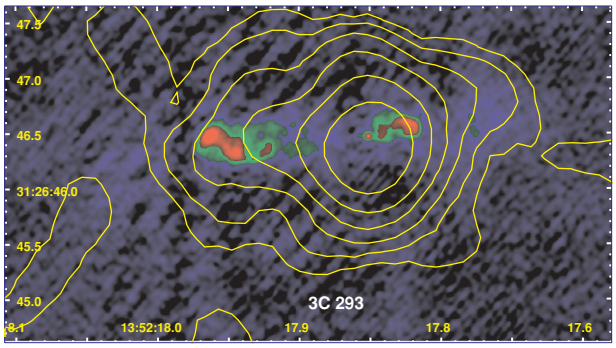

Figure 6. 3C 293. A 4.86 GHz radio image from a MERLIN observation which shows the brighter, inner radio structure. The X-ray contours come from a rebinned image as in Figure 1. The smoothing function is a Gaussian of FWHM = 0.″6. Contours begin at 0.05 counts pixel^{-1} and increase by factors of 2. (Radio map available on the Merlin archive.)

(A color version of this figure is available in the online journal.)

3.3. Source Details

3C 17. This is a broad-line radio galaxy (BLRG; Buttiglione et al. 2009) at a redshift of $z = 0.219$ (Figure 4). The kpc-scale radio morphology is dominated on the southern side by a strongly curved jet, as described by Morganti et al. (1993, 1999). The northern side has lower brightness and does not have a well-defined jet. There is also much larger, low-brightness radio emission. 3C 17 has been described as a "transition object" between FR I and FR II by Venturi et al. (2000). The jet has a bright knot at 3.″7 from the nucleus while the curved part lies at about 11″. We found X-ray and optical emission from both these knots. The results of the X-ray analysis and the relevance of using the curvature in the jet as a diagnostic tool in understanding the nature of X-ray emission in jets, has been presented in Massaro et al. (2009b).

3C 18. This is a bright FR II BLRG (Tadhunter et al. 2002) at redshift $z = 0.188$. As shown in Table 2, the number of counts increased by 13% going from 2″ to 10″ radii; an indication of diffuse emission around its nucleus.

3C 20. This is an FR II HEG radio galaxy with evidence for significant intrinsic absorption (see Table 2 and/or Table 4).

3C 33.1. This is a broad-line object yet both of our estimates for absorption show an intrinsic column density of (4–5) $\times 10^{22}$ cm^{-2}. Generally, we would not expect heavy absorption for BLOs; perhaps this source is an example of absorption with an anomalously low gas-to-dust ratio (see Grandi et al. 2007).

3C 52. This is an FR II radio galaxy and the original *HST* image (de Koff et al. 2000) shows a convincing case of an obscuring dust disk. The radio map illustrates that the radio axis is approximately perpendicular to the dust disk. Deeper radio maps show that the extended radio emission of this source is X-shaped. In Table 3, we report the marginal X-ray detection of the northern hotspot.

3C 105. This is a classical FR II radio galaxy. The host galaxy is an NLRG with only nuclear emission lines (Baum et al. 1988; Smith & Heckman 1989; Tadhunter et al. 1993).

We detected X-ray emission from the core and southern hotspot, both from the location where the radio jet appears to enter the hotspot region, and from the brightest radio emission at the terminal hotspot itself. It would seem that the jet, which has stretched over some 400 kpc on the plane of the sky (undetected in both radio and X-rays), has gently bent as it approaches the hotspot and is presumably finally much closer to the line of sight (l.o.s.) since the ratio of X-ray to radio intensity is about 10 times

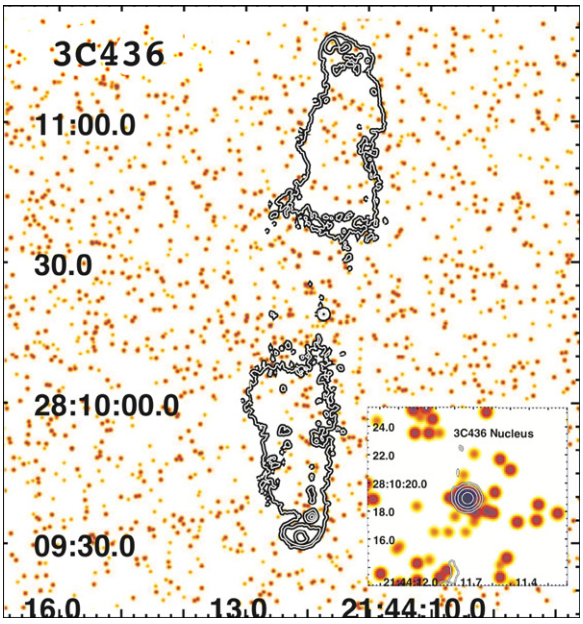

Figure 7. 3C 436. Flux map: f4; FWHM = 0.″5. 8.44 GHz radio contours: 0.125 mJy beam^{-1}, increasing by factors of 4. The insert shows the nucleus from an f4 flux map smoothed with a Gaussian of FWHM = 0.″5. (Radio map kindly supplied by M. Hardcastle).

(A color version of this figure is available in the online journal.)

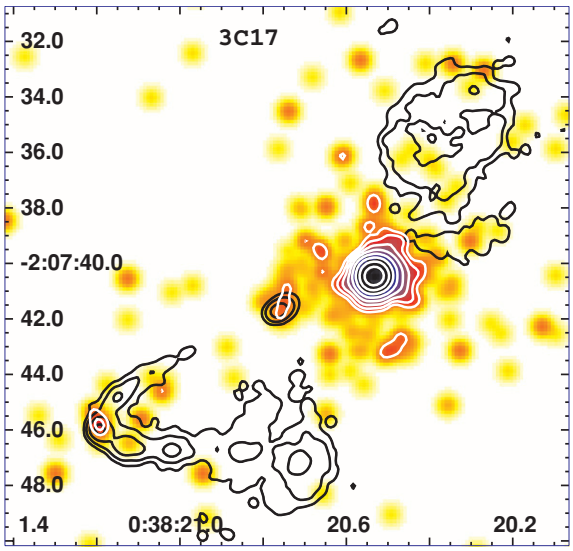

Figure 8. 3C 17. The *Chandra* flux map (0.5–7 keV) has been rebinned by a factor of 4 ("f4") and smoothed with a Gaussian of FWHM = 0.″5. X-ray contours start at 1×10^{-16} and increase by factors of 2. The 5 GHz radio map is from the VLA and has a restoring beam with FWHM = 0.″4. Radio contours start at 0.5 mJy beam^{-1} and increase by factors of 4. (Radio map kindly supplied by R. Morganti.)

(A color version of this figure is available in the online journal.)

larger at this "jet entrance" than for the hotspot itself. An image of this hotspot is shown in Figure 3 and a more detailed study of 3C 105 is in preparation (Orienti et al. 2010).

Both the photometric and the spectral analyses of the nuclear emission in 3C 105 are in agreement showing evidences of high intrinsic absorption. For this source, there are *Swift* and *XMM-Newton* public observations, we reduced and analyzed these data to compare our methods with a more accurate spectral analysis.

In the *XMM-Newton* observation, we found that the best-fit value of the intrinsic absorption is (49.1 ± 4.7) $\times 10^{22}$ cm^{-2} and

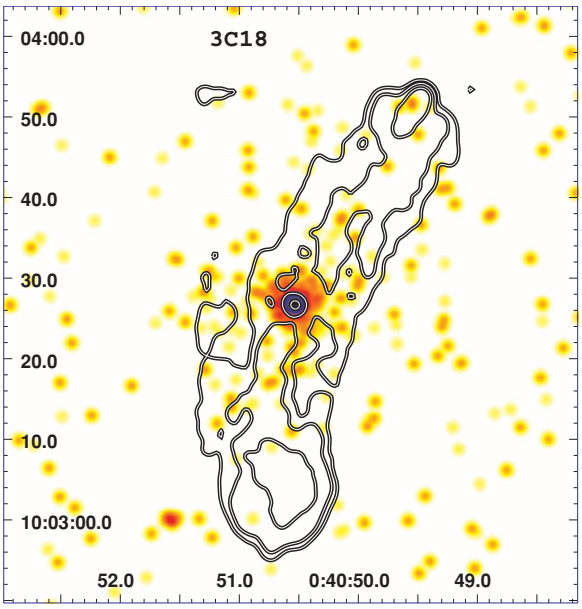

Figure 9. 3C 18. The *Chandra* flux map (0.5–7 keV) has been rebinned by a factor of 4 ("f4") and smoothed with a Gaussian of FWHM = 1″. The 1.4 GHz radio map is from the VLA and has a restoring beam with FWHM = 1.″7. Radio contours start at 2 mJy beam^{-1} and increase by factors of 4. (Radio map available on NED.)

(A color version of this figure is available in the online journal.)

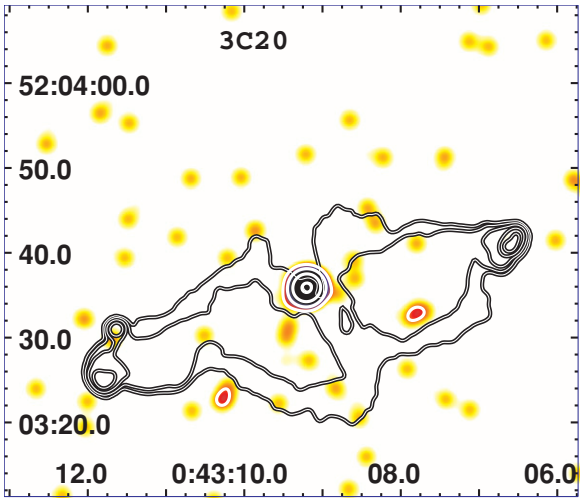

Figure 10. 3C 20. Flux map: f4; FWHM = 2″; contours start at 1e−17 and increase by factors of 4. Radio contours (8.4 GHz) start at 0.5 mJy beam^{-1} and increase by factors of 4. (Radio map kindly supplied by M. Hardcastle.)

(A color version of this figure is available in the online journal.)

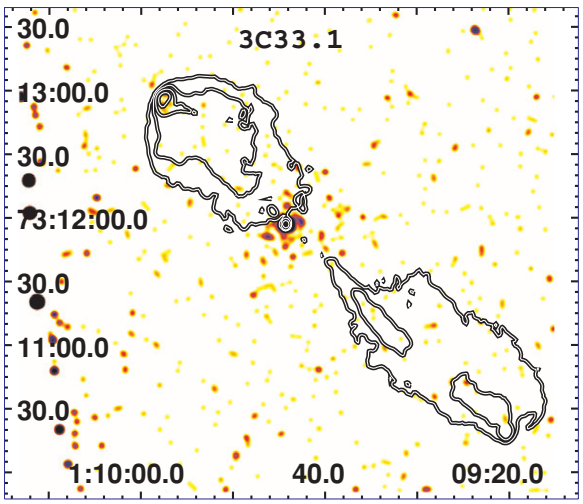

Figure 11. 3C 33.1. Flux maps: f2; FWHM = 6.″3. Radio (4.85 GHz) contours: 0.25 mJy beam^{-1}, increasing by a factor of 4. (Radio map kindly supplied by M. Hardcastle.)

(A color version of this figure is available in the online journal.)

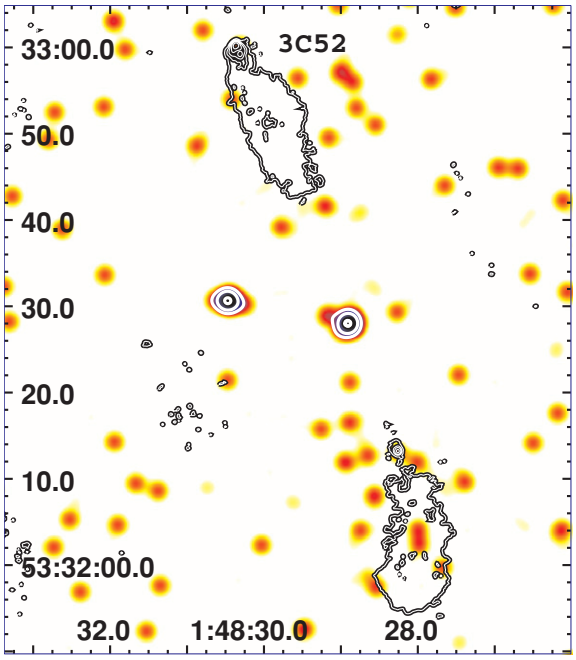

Figure 12. 3C 52. Flux map: f2; FWHM = 2″; contours start at 1e−17 and increase by a factor of 2. Radio contours: 0.25 mJy beam^{-1}, increasing by a factor of 4. They come from the VLA at 8 GHz with a beam size of 0.″38. (Radio map available on the NVAS archive.)

(A color version of this figure is available in the online journal.)

also a marginal detection of an iron Kα line with EW $\sim$ 90 eV in a complex X-ray spectrum similar to that of 3C 33 (Torresi et al. 2009) and 3C 234 (Piconcelli et al. 2008). The value of the intrinsic absorption found in the *Swift* data is consistent with that of *XMM-Newton*, with N_H equal to (30.4 $\pm$ 5.5) $\times$ 10^{22} cm^{-2}. All the details on this spectral analyses are reported in Appendices A and B.

3C 132. This is an FR II LEG radio galaxy with evidence for significant intrinsic absorption (see Table 2 and/or Table 4).

3C 165. 3C 165 is an FR II radio galaxy. We detected only the nucleus at a position $\approx$ 11″ from the NED location. G. Taylor (2009, private communication) provided a radio position for a point-like source ($\approx$ 9 mJy) from a recent 8.4 GHz VLA observation (J2000 6 43 6.660 + 23 19 0.55). Our X-ray position agrees with this so we believe it is the nucleus of the radio galaxy.

3C 171. This is a small FR II radio galaxy. It has a slightly disturbed elliptical morphology and particularly strong extended emission-line regions. These emission-line regions are aligned with the radio emission (Heckman et al. 1984; Blundell 1996). We detect extended X-ray emission around the nucleus consistent with a hot gas component because there is no one-to-one association with the radio emission, and the nucleus is also strongly depolarized (Hardcastle et al. 2003). We also found X-rays associated with the western hotspot. An analysis based on a *Chandra* follow-up observation of 3C 171 uses radio polarization data to interpret the extended

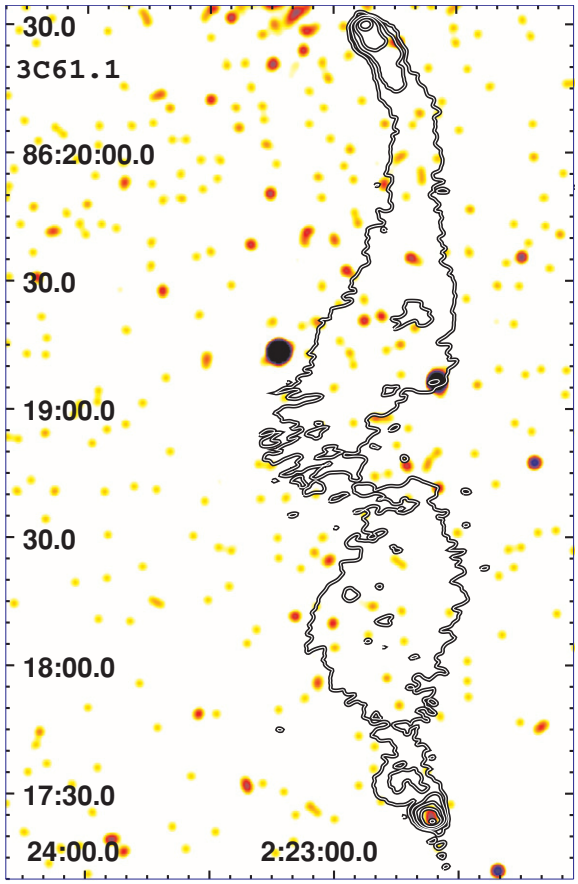

Figure 13. 3C 61.1. Flux map: FWHM = 1″. Radio (4.86 GHz) contours: 0.5 mJy beam^{-1}, increasing by a factor of 4. (Radio map kindly supplied by M. Hardcastle.)

(A color version of this figure is available in the online journal.)

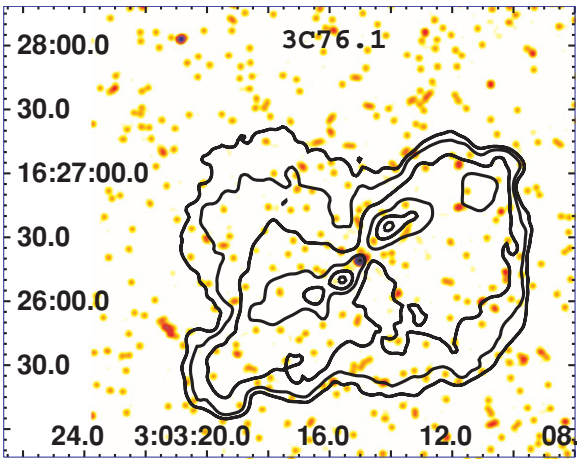

Figure 14. 3C 76.1. Flux map: f2: FWHM = 6″.1.5 GHz radio contours start at 1 mJy beam^{-1} and increase by a factor of 2. (Radio map available on the website: http://www.jb.man.ac.uk/, "An Atlas of DRAGNs".)

(A color version of this figure is available in the online journal.)

X-ray emission (Hardcastle et al. 2010). We find evidence for significant intrinsic absorption (see Table 2 and/or Table 4).

3C 184.1. This is a broad-line object yet both of our estimates for absorption show an intrinsic column density of (4–5) × 10^{22} cm^{-2}. In this respect, it is similar to 3C 33.1.

3C 223.1. This is an FR II HEG radio galaxy with an X-shaped radio morphology. In this source, we find evidence for significant intrinsic absorption (see Table 2 and/or Table 4).

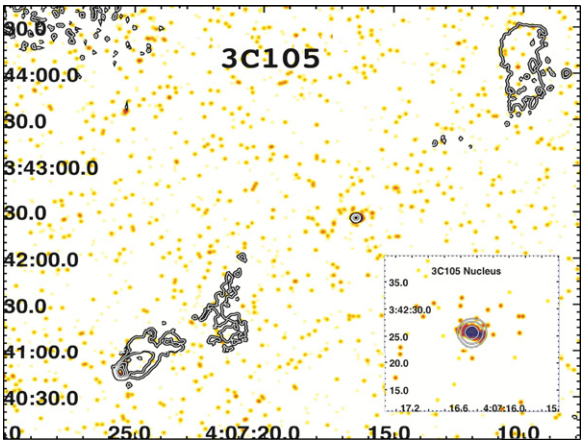

Figure 15. 3C 105. Figure 3 gives an enlarged view of the southern hotspot. Flux map: f1; FWHM = 2″.8.4 GHz radio contours: 0.5 mJy beam^{-1}, increasing by a factor of 4. The inset shows the nucleus from an f4 Flux map smoothed with a Gaussian of FWHM = 0″.5. (Radio map kindly supplied by M. Hardcastle.)

(A color version of this figure is available in the online journal.)

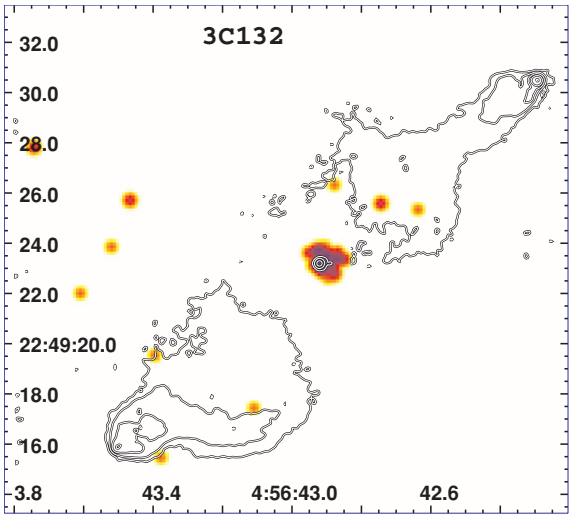

Figure 16. 3C 132. Flux map: f4; FWHM = 0″.25. Radio (8.44 GHz) contours: 0.125 mJy beam^{-1}, increasing by a factor of 4. (Radio map kindly supplied by M. Hardcastle.)

(A color version of this figure is available in the online journal.)

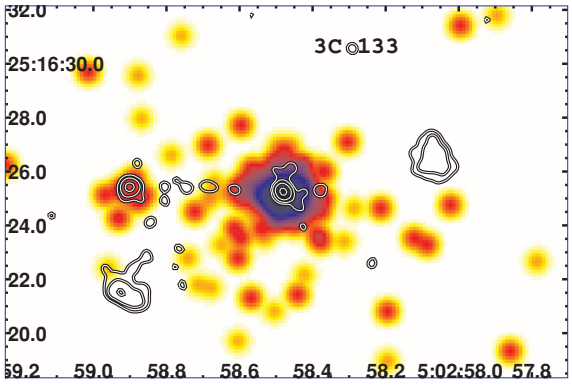

Figure 17. 3C 133. Flux map: f4; FWHM = 0″.5. 4.89 GHz radio contours: 10 mJy beam^{-1}, increasing by factors of 4. (Radio map available on the NVAS archive.)

(A color version of this figure is available in the online journal.)

3C 287.1. This is a strongly core-dominated FR II BLRG with a very similar radio structure to 3C 171. No hotspot has

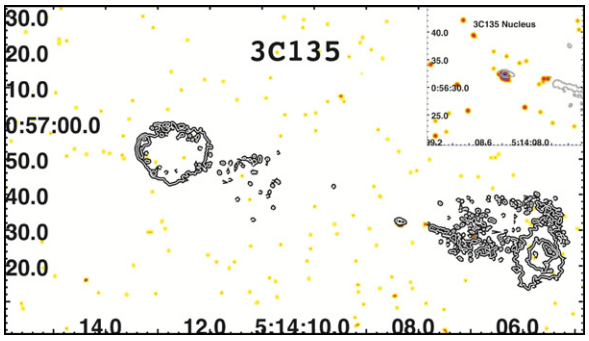

Figure 18. 3C 135. Flux map: f2; FWHM = 1.″8.46 GHz radio contours: 0.125 mJy beam^{-1}, increasing by a factor of 4. The insert shows the nucleus from an f4 Flux map smoothed with a Gaussian of FWHM = 0.″5. (Radio map kindly supplied by M. Hardcastle.)

(A color version of this figure is available in the online journal.)

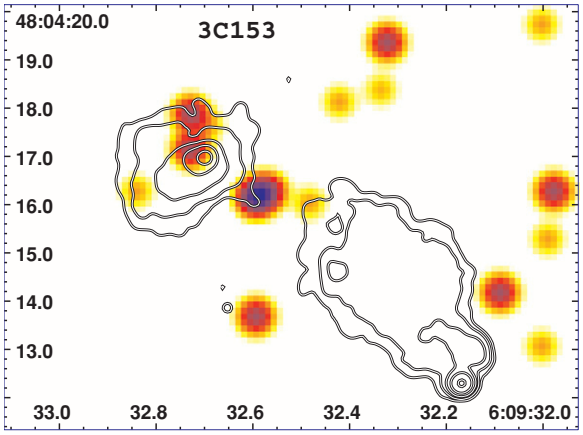

Figure 19. 3C 153. Flux map: f4; FWHM = 0.″5. 8.41 GHz radio contours: 0.5 mJy beam^{-1}, increasing by a factor of 4. (Radio map kindly supplied by M. Hardcastle.)

(A color version of this figure is available in the online journal.)

been detected in the X-rays but only the bright nucleus. As in the case of 3C 18, it may be considered an example of diffuse emission around the core. The number of counts increases by about 11% going from a circular region of $r = 2''$ to $10''$. This could be due to hot gas around the nuclear region similar to the case of 3C 18.

3C 293. This has a poorly defined X-ray nucleus precluding precise registration, due to an excess of extended emission. Therefore, we are uncertain if the small X-ray extension to the east of the nucleus is emission from the radio jet or if it lies along the northern edge of the jet. An image is shown in Figure 6.

Very Long Baseline Interferometry (VLBI) observations (Giovannini et al. 2005, 2008) show a two-sided structure with symmetric jets. The jet emission is detected on both sides up to ∼20 mas from the core, with the eastern jet being slightly brighter. We refer to it as the main jet (J), and to the western one as the counterjet (CJ). This is also in agreement with the description of Beswick et al. (2004), although their suggested jet orientation and velocity are in contrast with the high symmetry of the VLBA jet. From a comparison between different images (Giovannini et al. 2008) we find that the sub-arcsecond structure in the E–W direction is clearly related to a restarted activity of the central AGN; however, the large change in position angle (PA) with respect to the extended lobes is not due to a PA change in the restarted nuclear activity but it looks constant in time and it is likely produced by the jet interaction with a rotating disk

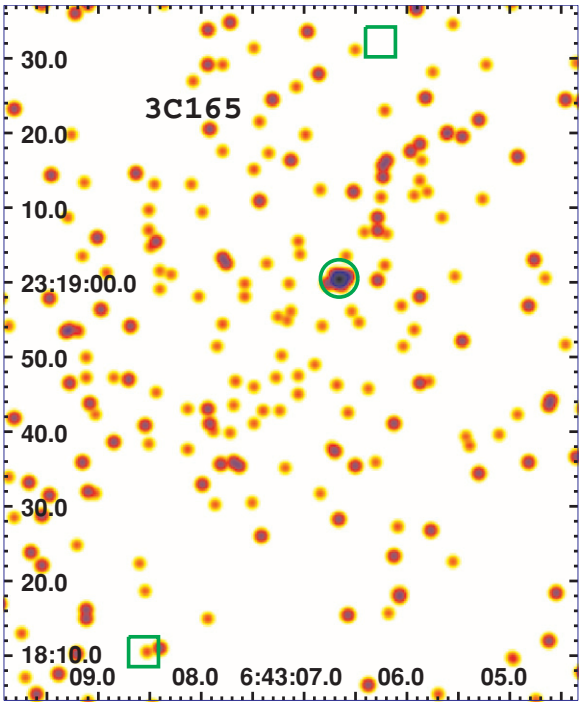

Figure 20. 3C 165. Unfortunately, we were unable to obtain a meaningful radio map. The X-ray image is an f2 version of the total band flux map, smoothed with a Gaussian of FWHM = 1″. The circle marks the location of the quasi-unresolved radio source we take to be the nucleus (see the text). The two squares show the approximate locations of the *N* and *S* hotspots taken from a jpeg picture found on NED (an early VLA observation at 1.6 GHz included in Leahy & Williams 1984.)

(A color version of this figure is available in the online journal.)

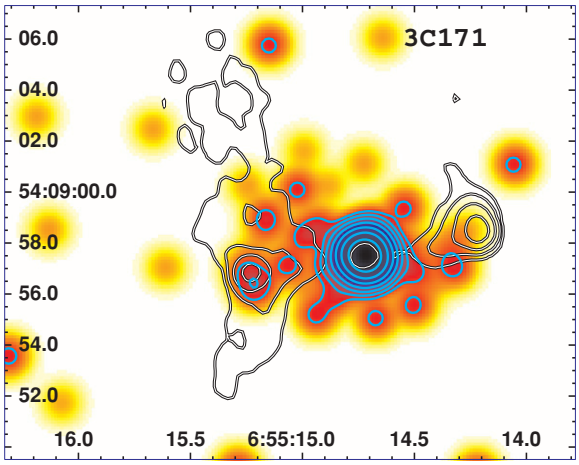

Figure 21. 3C 171. Flux map: f4; FWHM = 1″; contours start at 2e−17 and increase by a factor of 2. 8.0 GHz radio contours: 1 mJy beam^{-1}, increasing by a factor of 4. (Radio map kindly supplied by M. Hardcastle.)

(A color version of this figure is available in the online journal.)

as discussed by van Breugel et al. (1984). In this scenario, we expect that the jet at ∼2.5 kpc from the core is no longer relativistic. We find evidence for significant intrinsic absorption (see Table 2 and/or Table 4).

3C 303.1. O'Dea et al. (2006) analyzed *XMM-Newton* data and suggested that the spectrum was consistent with a contribution from hot gas which had been shocked by the radio source. The *Chandra* data show X-ray emission elongated along the radio source axis and with a size comparable to that of the radio source consistent with this interpretation. The source is very

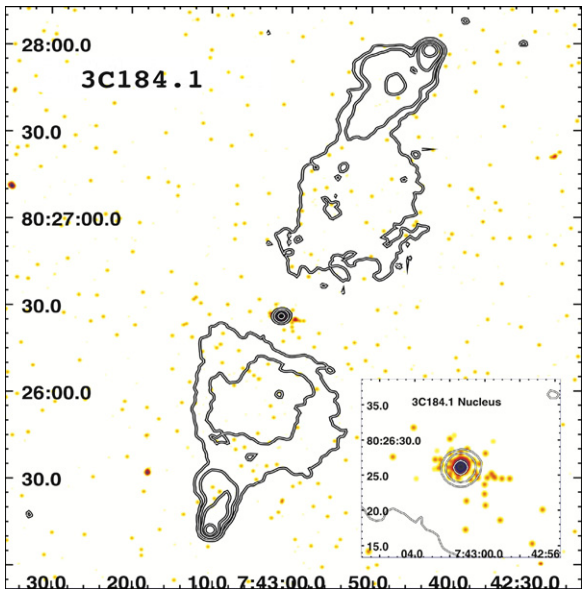

Figure 22. 3C 184.1. Flux map: f2; FWHM = 1″. Radio contours (VLA, 8 GHZ): 0.25 mJy beam^{-1}, increasing by a factor of 4. The insert shows the nucleus from an f4 Flux map smoothed with a Gaussian of FWHM = 0.″5 (Radio map available on the Web site: http://www.jb.man.ac.uk/, "An Atlas of DRAGNs".)

(A color version of this figure is available in the online journal.)

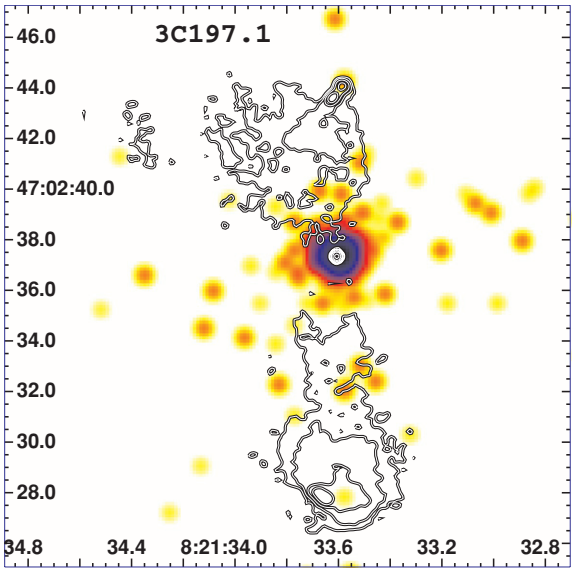

Figure 23. 3C 197.1. Flux map: f4; FWHM = 0.″5. Radio (8.46 GHz) contours: 0.125 mJy beam^{-1}, increasing by a factor of 2. (Radio map kindly supplied by M. Hardcastle.)

(A color version of this figure is available in the online journal.)

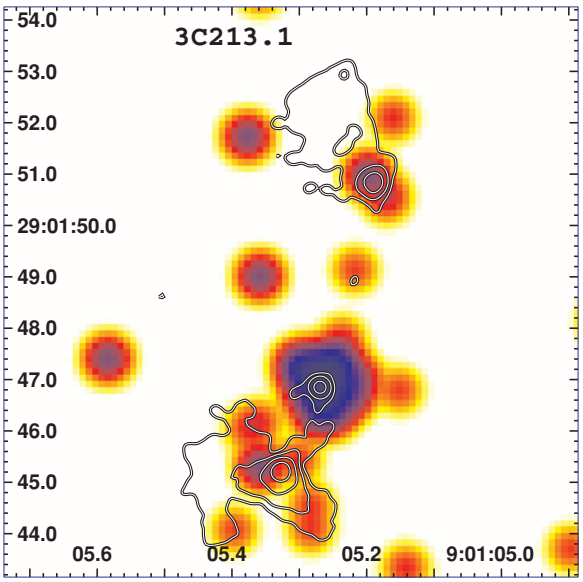

Figure 24. 3C 213.1. Flux map: f4; FWHM = 0.″5. Radio contours (VLA, 8 GHZ): 0.5 mJy beam^{-1}, increasing by factors of 4. (Radio map available on the NVAS archive.)

(A color version of this figure is available in the online journal.)

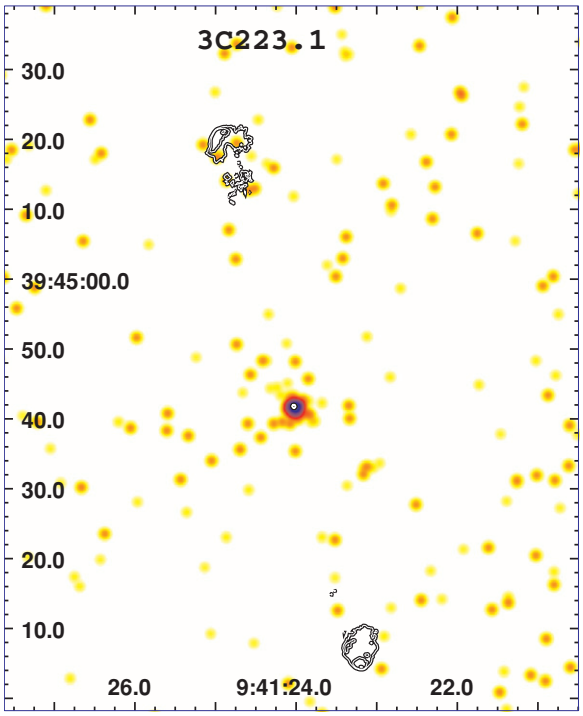

Figure 25. 3C 223.1. Flux map: f4; FWHM = 1″. Radio (8.46 GHz) contours: 0.125 mJy beam^{-1}, increasing by factors of 4.

(A color version of this figure is available in the online journal.)

small and it is hard to separate the nuclear component from the extended emission.

3C 305. This is a relatively low-power radio galaxy located at redshift $z \sim 0.0416$ (see Figure 1). It has been classified as a peculiar FR I on the basis of the radio power and morphology (Heckman et al. 1982) and presents a prominent extended emission-line region of roughly the same dimension as the radio structure. It is one of the more interesting sources in our sample, because it is an FR I–CSS source in which the X-ray emission is not coincident with the radio, but there is clear evidence for an association between the X-ray emission and [O III]5007. A detailed comparison of the radio, optical, and X-ray images (here reported) of 3C 305 is used to elucidate the nature of the emitting gas in Massaro et al. (2009a).

3C 323.1. This is a quasar with a bright nucleus in the X-rays. The radio morphology is that of a classical FR II but no hotspots have been detected in the X-ray band. Similar to the cases of 3C 18 and 3C 287.1, this source is a good example of diffuse emission around the nucleus. The number of counts increases by 25% going from a circular region of $r = 2''$–$10''$.

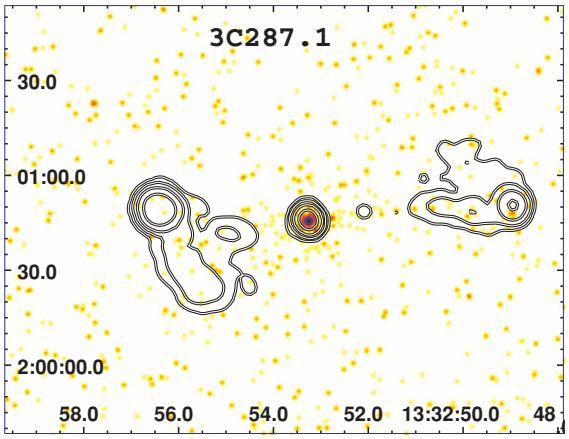

Figure 26. 3C 287.1. Flux map: f2; FWHM = 1″.1.6 GHz radio contours: 2 mJy beam^{-1}, increasing by factors of 4. (Radio map available on the NVAS archive.)

(A color version of this figure is available in the online journal.)

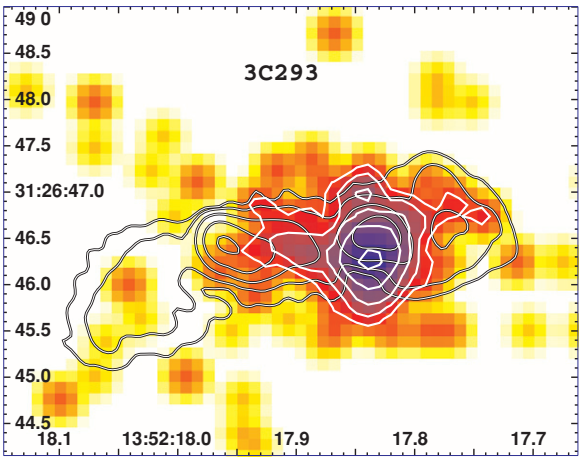

Figure 27. 3C 293. Flux map: f4: FWHM = 0″.25; contours start at 5e−16 and increase by a factor of 2. Radio contours: 1 mJy beam^{-1}, increasing by factors of 4. The registration (alignment of radio and X-ray nuclei) is problematic for this source. (Radio map available on the Merlin archive.)

(A color version of this figure is available in the online journal.)

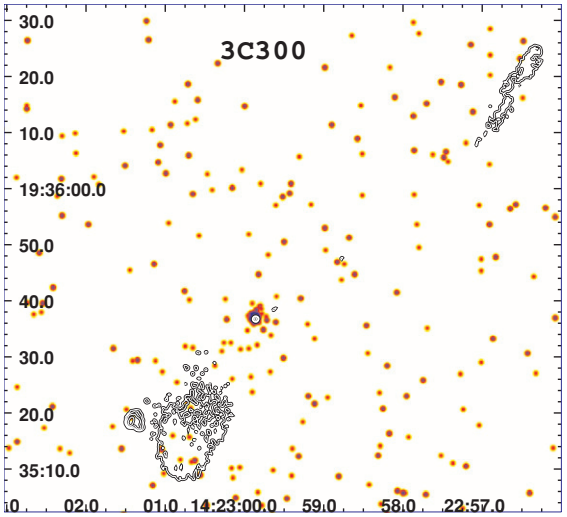

Figure 28. 3C 300. Flux map: f4: FWHM = 0″.5. 8.06 GHz radio contours: 0.25 mJy beam^{-1}, increasing by factors of 4. (Radio map kindly supplied by M. Hardcastle.)

(A color version of this figure is available in the online journal.)

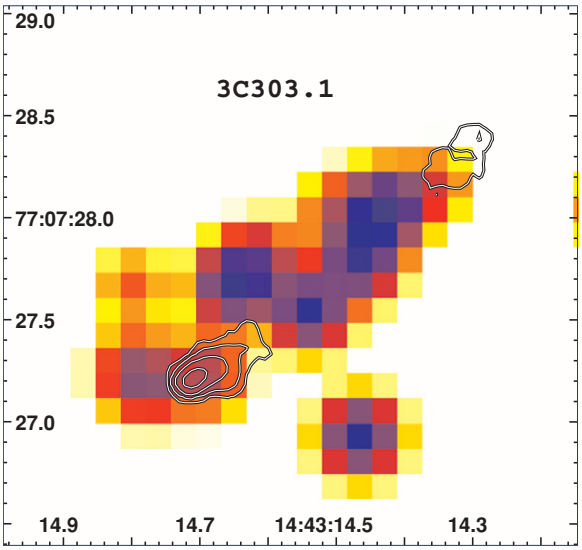

Figure 29. 3C 303.1. Flux map: f4; FWHM = 0″.25. 5.0 GHz radio contours: 1 mJy beam^{-1}, increasing by factors of 4. (Radio map available on the Merlin archive.)

(A color version of this figure is available in the online journal.)

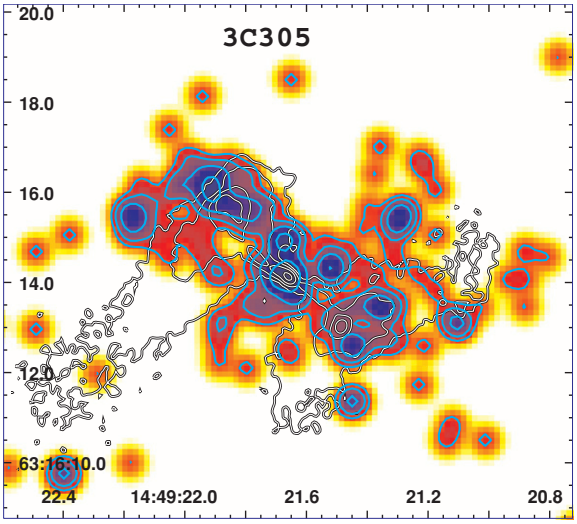

Figure 30. 3C 305. Flux map: f4; FWHM = 0″.5; contours start at 2e−17 and increase by factors of 2. 1.5 GHz radio contours: 0.5 mJy beam^{-1}, increasing by factors of 4. (Radio map available on the Merlin archive.)

(A color version of this figure is available in the online journal.)

3C 332. This is a powerful FR II radio galaxy with a prominent quasar-like infrared nucleus marking the center of an elliptical host galaxy. This source has a clear detection of diffuse emission around the nucleus. The number of counts increases by 42% going from a circular region of $r = 2''$–$10''$ both centered on the radio position of the core. We find evidence for significant intrinsic absorption (see Table 2 and/or Table 4).

3C 349. This is an FR II radio galaxy that lies at redshift $z = 0.205$. We detect the southern hotspot and there appears to be two components, so it might be similar to the S hotspot of 3C 105.

3C 381. This is an FR II HEG radio galaxy with evidence for significant intrinsic absorption (see Table 2 and/or Table 4).

3C 436. This is an FR II HEG radio galaxy with evidence for significant intrinsic absorption (see Table 2 and/or Table 4).

3C 460. This is not well registered since the only available (to us) radio map does not detect the nuclear emission; however,

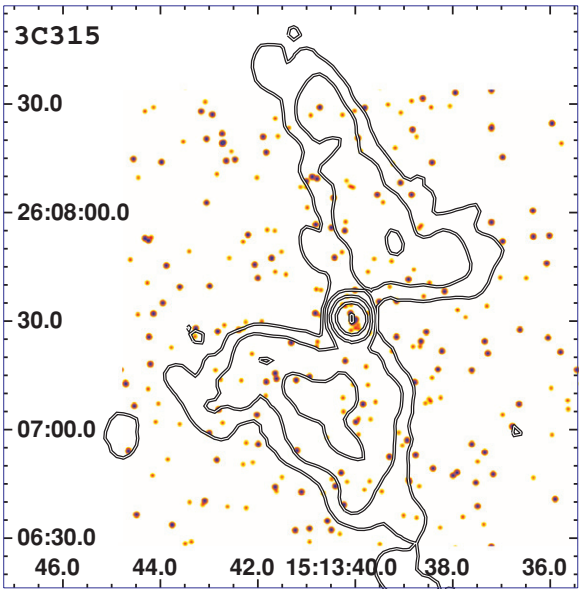

Figure 31. 3C 315. Flux map: f4; FWHM = 1.″1.43 GHz radio contours: 1 mJy beam^{-1}, increasing by factors of 4. (Radio map available on the website: http://www.jb.man.ac.uk/, "An Atlas of DRAGNs".)

(A color version of this figure is available in the online journal.)

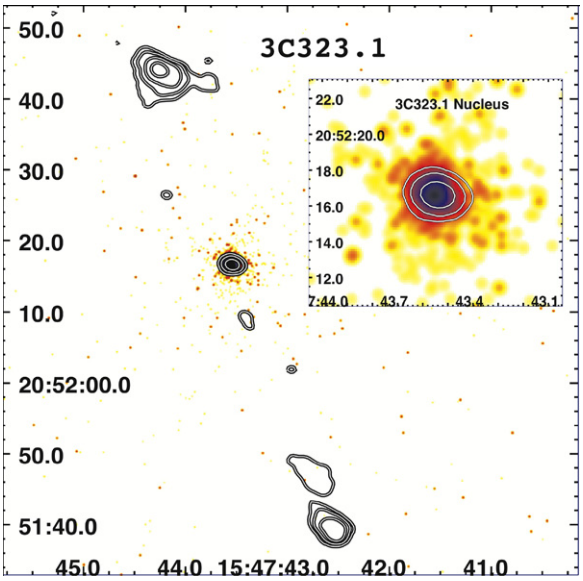

Figure 32. 3C 323.1. Flux map: f4; FWHM = 0.″25. 4.9 GHz radio contours: 1 mJy beam^{-1}, increasing by factors of 4. The insert shows the nucleus from an f4 Flux map smoothed with a Gaussian of FWHM = 0.″5 (Radio map available on the NVAS archive.)

(A color version of this figure is available in the online journal.)

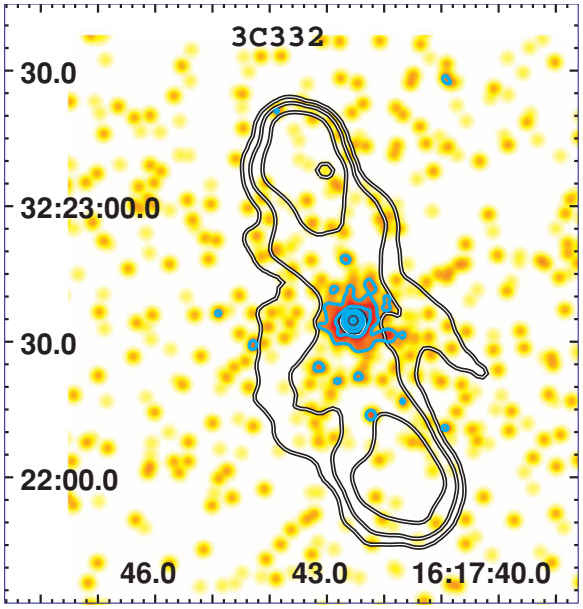

Figure 33. 3C 332. Flux map: f4; FWHM = 2″; contours start at 1e−17 and increase by factors of 2. Radio (5 GHz) contours: 0.5 mJy beam^{-1}, increasing by factors of 4. (Radio map available on the NVAS archive.)

(A color version of this figure is available in the online journal.)

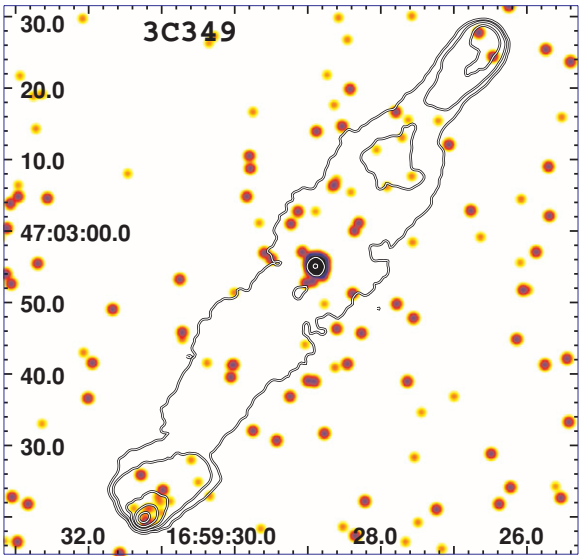

Figure 34. 3C 349. Flux map: f4; FWHM = 1.″1.5 GHz radio contours: 1 mJy beam^{-1}, increasing by factors of 4. (Radio map available on the website: http://www.jb.man.ac.uk/, "An Atlas of DRAGNs".)

(A color version of this figure is available in the online journal.)

the core is clearly detected in the X-rays, as shown in Figure 7. There is a single event coincident with the N hotspot, and two counts near the S (brighter in radio) hotspot.

4. SUMMARY

We have presented our analyses of the *Chandra* 3C Snapshot Survey. Our goal is to obtain X-ray data for all extragalactic 3C sources with $z < 0.3$ so as to have a complete, unbiased sample. Our AO9 proposal resulted in the current new data for 30 of the (then) unobserved 60 sources not already in the archive with exposures of 8 ks or greater. We will submit a *Chandra* proposal for AO12 in order to complete the sample. When the remaining 27 are observed, it will then be possible to have a complete sample by recovering many more 3C sources from the archives.

We have constructed flux maps for all the observations and given photometric results for the nuclei and radio hotspots. For the stronger nuclei, we have employed the usual spectral analysis, and compared the column densities of intrinsic absorption to those obtained from the ratio of hard to medium fluxes. As expected, we find a sizable fraction (1/3) of our sources showing evidence for significant absorption ($N_H > 5 \times 10^{22}$ cm^{-2}). In particular, for 3C 105, we analyzed the archival observations performed by *XMM-Newton* and *Swift* and we found that its core is absorbed and these spectra are in agreement with our *Chandra* spectral analysis. We also found a marginal

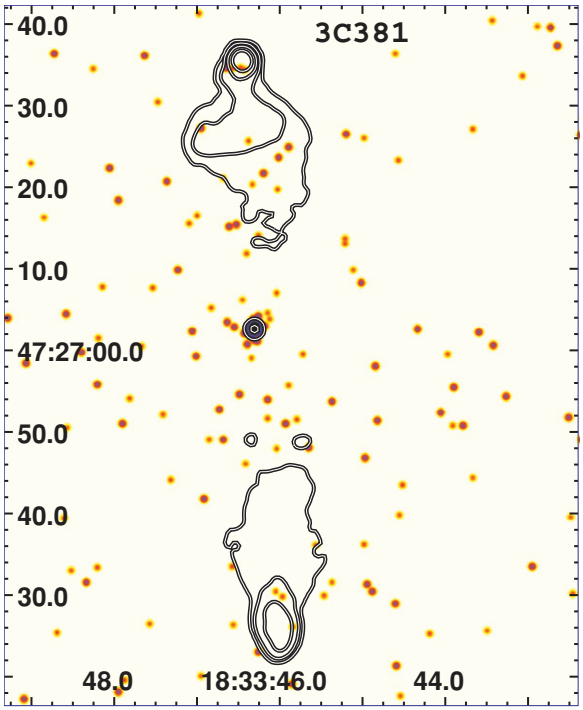

Figure 35. 3C 381. Flux map: f4; FWHM = 0.″5. 8.44 GHz radio contours: 1 mJy beam^{-1}, increasing by factors of 4. (Radio map kindly supplied by M. Hardcastle.)

(A color version of this figure is available in the online journal.)

detection of the Fe Kα emission line and evidence of a soft X-ray excess.

We have found several sources worthy of more detailed study, and with collaborators have published papers on 3C 17, 3C 171, and 3C 305. Our decision to waive proprietary rights has permitted others (e.g., Hardcastle et al. 2009, 2010) to use relevant data in a timely manner, and we intend to continue this policy in our *Chandra* AO12 proposal for the remaining unobserved sources.

We thank the anonymous referee for useful comments that led to improvements in the paper. We are extremely grateful to S. Bianchi for his help in the *XMM-Newton* data reduction procedure and analysis of the X-ray spectrum of 3C 105 and to M. L. Conciatore for her suggestions in the use of *Swift–XRT* data for the same source. We thank R. Morganti for giving us her 5 GHz VLA map of 3C 17, R. Beswick for that of 3C 293, and A. Tilak for the *HST* images of 3C 171. We are grateful to M. Hardcastle for providing several radio maps of the 3C sources. This research has made use of NASA's Astrophysics Data System; SAOImage DS9, developed by the Smithsonian Astrophysical Observatory; and the NASA/IPAC Extragalactic Database (NED), which is operated by the Jet Propulsion Laboratory, California Institute of Technology, under contract with the National Aeronautics and Space Administration. Several radio maps were downloaded from the NVAS. The National Radio Astronomy Observatory is operated by Associated Universities, Inc., under contract with the National Science Foundation. Several radio maps have been provided by the Merlin archive. The work at SAO is supported by NASA-GRANT GO8-9114A and the work at RIT was supported by *Chandra* grant GO8-9114C. F. Massaro acknowledges the Foundation BLANCEFLOR Boncompagni-Ludovisi, n'ee Bildt for the grant awarded him in 2009.

Facilities: VLA, MERLIN, *HST*, *CXO* (ACIS), *XMM* (EPIC PN), *Swift* (XRT)

Note added in proof. While the manuscript was in press, we identified five sources as being affected by pileup (0.5 to 1 count/frametime). These are marked with an asterisk in Tables 2 and 4. Generally, our net counts, fluxes, and luminosities for these sources will be underestimated, and the ratios (hard/medium) will tend to be larger than they should be (Table 2). In Table 4, the effects of pileup will generally be that the estimated spectral index will be smaller than it should be.

APPENDIX A

IMAGES OF THE SOURCES

We report all the images of our sample in Figures 8–35. Although for many of our sources the X-ray data are comprised of rather few counts, we show here the radio morphology via contour diagrams which are superposed on X-ray flux maps that have been smoothed with a Gaussian. The full width at half-maximum (FWHM) of the Gaussian smoothing function is given in the figure captions and varies between 0.″25 and 2″. When there is sufficient signal-to-noise ratio (S/N) of the X-ray image to provide spatial information, we have added contours (cyan or white) which are normally separated by factors of 2. Most of the overlayed radio contours increase by factors of 4. Our standard X-ray flux maps have been rebinned by a factor of 4 ("f4") to give a pixel size of 0.″123. For radio sources of large angular extent, we occasionally use f2 instead of f4 in order that our standard array size of 1024 covers the entire source. Brightness units of the flux maps are erg cm^{-2} s^{-1} pixel^{-1}. The primary reason figures appear so different from each other is the wide range in angular size of the radio sources.

APPENDIX B

SPECTRAL ANALYSIS OF THE NUCLEAR EMISSION IN 3C 105

The data reduction has been performed following the procedures described by Massaro et al. (2008a, 2008b) and Bianchi et al. (2009) both for the *Swift* and *XMM-Newton* data. Here we report only the basic parameters used on the data reduction.

B.1. Swift Observations

3C 105 has been observed by *Swift* four times between 2006 July 11 and 16 (Obs ID 00035625001-2-3-4), operating with all the instruments in data taking mode and with an exposure of about 7, 3, 4, and 5 ks, respectively. We added all these observation to increase the S/N.

For our analysis, we considered only *Swift–XRT* (Burrows et al. 2005) data. The *Swift–XRT* data analysis has been performed with the XRTDAS software distributed within the HEAsoft package (v. 6.8.0). Event files were calibrated and cleaned with standard filtering criteria using the XRTPIPELINE task, combined with the latest calibration files available in the *Swift* CALDB distributed by HEASARC. Events in the energy range 0.3–10 keV with grades 0–12 (photon counting (PC) mode) were used in the analyses (see Hill et al. 2004 for a description of readout modes). No signatures of pile-up were found in our *Swift* observations. Events are extracted using a 20 pixel radius circle. The background for PC mode is estimated from a nearby source-free circular region of 20 pixel radius.

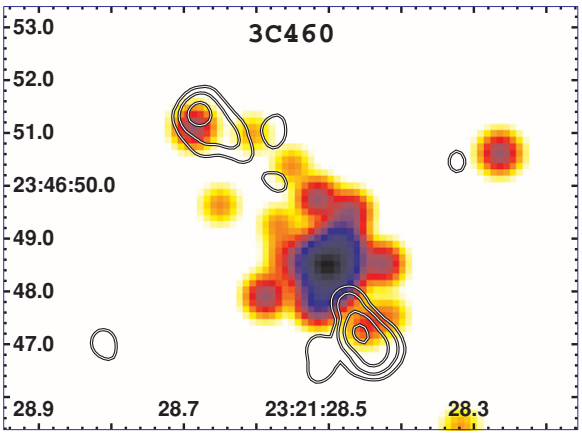

Figure 36. 3C 460. Flux map: f4; FWHM = 0.″5. 4.89 GHz radio contours: 1 mJy beam^{-1}, increasing by factors of 4. (Radio map available on the NVAS archive.)

(A color version of this figure is available in the online journal.)

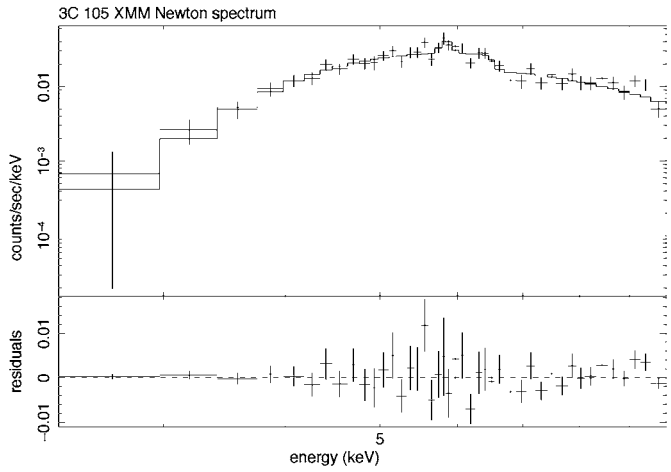

Figure 37. *XMM-Newton* EPIC-PN spectrum of the nuclear emission in 3C 105 with its residuals, fitted with the best-fit model.

B.2. XMM-Newton Observations

3C 105 was observed with *XMM-Newton* (ObS ID 0500850401) on 2008 August 25 with all EPIC CCD cameras: the EPIC-PN (Struder et al. 2001), and EPIC-MOS (Turner et al. 2001), operating in Full frame mode and with Thin filter. Only EPIC-PN data are reported in this work, the EPIC-MOS data have been reduced and analyzed and we found them in agreement with our results.

Extractions of all light curves, source, and background spectra are done using the *XMM-Newton* Science Analysis System (SAS) v9.0.0. The calibration index file (CIF) and the summary file of the observation data file (ODF) were generated using updated calibration files (CCF) following the "User's Guide to the *XMM-Newton* Science Analysis System" (issue 3.1; Loiseau et al. 2004) and "The *XMM-Newton* ABC Guide" (v. 2.01; Snowden et al. 2004). Event files were produced by the *XMM-Newton* EPCHAIN pipeline.

Photons are extracted from a circular region. The typical value of the external radius for the circular region is 14″. A restricted energy range (0.5–10 keV) is used to avoid possible residual calibration uncertainties.

To ensure the validity of χ^2 statistics, both spectra, *Swift* and *XMM-Newton*, are grouped by combining instrumental channels so that each new bin comprises 30 counts or more, well above the limit for the χ^2 test applicability (Kendall & Stuart 1979).

B.3. Spectral Analysis

We initially fitted the *XMM-Newton* spectrum in the energy range 2–10 keV with a model composed by: the galactic absorption (see Table 1), a power law (spectral index $\alpha = 0.83 \pm 0.25$), an intrinsic absorption ($N_H^{\rm int} = (49.1 \pm 4.7) \times 10^{22}$ cm^{-2}) plus an intrinsic narrow iron Kα emission line (Gaussian profile, at energy $E_{\rm K\alpha} = 6.36 \pm 0.05$ keV). In Figure 36, the *XMM-Newton* spectrum in the 2–10 keV energy range is shown, the χ^2 for the model proposed is 36.7 over 38 degrees of freedom (dof). We also found evidence of a soft excess at energies below 2 keV, that could be due to a blend of emission lines as the case of other radio galaxies (e.g., 3C 33: Torresi et al. 2009; 3C 234: Piconcelli et al. 2008) or it could be interpreted as soft X-ray emission from the inner jet of the host radio galaxy. Finally, both *Swift–XRT* and *XMM-Newton* spectral analysis are in agreement indicating evidences of intrinsic absorption, however the low S/N of the *Swift–XRT* observation does not allow a good estimate of its value. The photometric and the spectral method in this case are not in agreement because the spectral analysis revealed a more detailed spectrum than a simple featureless power-law continuum. The *XMM-Newton* spectrum of the nuclear emission of 3C 105 is shown in Figure 37.

REFERENCES

Alexander, D. M., et al. 2001, AJ, 122, 2156
Alexander, D. M., et al. 2002, AJ, 123, 1149
Arnaud, K. A. 1996, in ASP Conf. Ser. 101, Astronomical Data Analysis Software and Systems V, ed. G. Jacoby & J. Barnes (San Francisco, CA: ASP), 17
Baum, S. A., Zirbel, E. L., & O'Dea, C. P. 1995, ApJ, 451, 88
Baum, S. A., et al. 1988, ApJS, 68, 643
Beswick, R. J., Peck, A. B., Taylor, G. B., & Giovannini, G. 2004, MNRAS, 352, 49
Bianchi, S., et al. 2009, A&A, 495, 421
Blundell, K. M. 1996, MNRAS, 283, 538
Bridle, A. H., & Perley, R. A. 1984, ARA&A, 22, 319
Burrows, D., et al. 2005, Space Sci. Rev., 120, 165
Buttiglione, S., Capetti, A., Celotti, A., Axon, D. J., Chiaberge, M., Macchetto, F. D., & Sparks, W. B. 2009, A&A, 495, 1033
Cash, W. 1979, ApJ, 228, 939
Chiaberge, M., Capetti, A., & Celotti, A. 2002, A&A, 394, 791
Cohen, M. H., Ogle, P. M., Tran, H. D., Goodrich, R. W., & Miller, J. S. 1999, AJ, 118, 1963
De Koff, S., et al. 2000, ApJS, 129, 33
Evans, D. A., Worrall, D. M., Hardcastle, M. J., Kraft, R. P., & Birkinshaw, M. 2006, ApJ, 642, 96
Fanaroff, B. L., & Riley, J. M. 1974, MNRAS, 167, 31
Floyd, D. J. E., Perlman, E., Leahy, J. P., Beswick, R. J., Jackson, N. J., Sparks, W. B., Axon, D. J., & O'Dea, C. P. 2006, ApJ, 639, 23
Garrington, S. T., Leahy, J. P., Conway, R. G., & Laing, R. A. 1988, Nature, 331, 147
Giovannini, G., Liuzzo, E., Giroletti, M., & Taylor, G. B. 2008, J. Phys.: Conf. Ser., 131, a2038
Giovannini, G., Taylor, G. B., Feretti, L., Cotton, W. D., Lara, L., & Venturi, T. 2005, ApJ, 618, 635
Giovannini, G., et al. 2001, ApJ, 552, 508
Grandi, P., Guainazzi, M., Cappi, M., & Ponti, G. 2007, MNRAS, 381, L21
Hardcastle, M. J. 2003, MNRAS, 339, 360
Hardcastle, M. J., Evans, D. A., & Croston, J. H. 2007, MNRAS, 376, 1849
Hardcastle, M. J., Evans, D. A., & Croston, J. H. 2009, MNRAS, 396, 1929
Hardcastle, M. J., Massaro, F., & Harris, D. E. 2010, MNRAS, 401, 2697
Harris, D. E., & Krawczynski, H. 2002, ApJ, 565, 244
Harris, D. E., & Krawczynski, H. 2006, ARA&A, 44, 63
Heckman, T. M., Miley, G. K., Balick, B., van Breugel, W. J. M., & Butcher, H. R. 1982, ApJ, 262, 529
Heckman, T. M., Van Breugel, W. J. M., & Miley, G. K. 1984, ApJ, 286, 509
Hill, J. E., et al. 2004, Proc. SPIE, 5165, 217

Hine, R. G., & Longair, M. S. 1979, MNRAS, 188, 111
Kalberla, P. M. W., Burton, W. B., & Hartmann, D. 2005, A&A, 440, 775
Kendall, M., & Stuart, A. 1979, The Advanced Theory of Statistics (New York: Macmillan)
Laing, R. A. 1981, MNRAS, 195, 261
Laing, R. A. 1988, Nature, 331, 149
Laing, R. A., Bridle, A. H., Parma, P., Feretti, L., Giovannini, G., Murgia, M., & Perley, R. A. 2008, MNRAS, 386, 657
Laing, R. A., Jenkins, C. R., Wall, J. V., & Unger, S. W. 1994, in ASP Conf. Ser. 54, The First Stromlo Symposium: The Physics of Active Galaxies, ed. G. V. Bicknell, M. A. Dopita, & P. J. Quinn (San Francisco, CA: ASP), 201
Leahy, J. P., & Williams, A. G. 1984, MNRAS, 210, 929
Liuzzo, E., et al. 2009, A&A, 505, 509
Loiseau, N., et al. 2004, User's guide to the *XMM-Newton* Science Analysis System (issue 3.1; Noordwijk: ESA)
Massaro, F., Tramacere, A., Cavaliere, A., Perri, M., & Giommi, P. 2008a, A&A, 478, 395
Massaro, F., et al. 2008b, A&A, 489, 1047
Massaro, F., et al. 2009a, ApJ, 692, L123
Massaro, F., et al. 2009b, ApJ, 696, 980
Miley, G. 1980, ARA&A, 18, 165
Morganti, R., Killeen, N. E. B., & Tadhunter, C. N. 1993, MNRAS, 263, 1023
Morganti, R., Oosterloo, T., & Tadhunter, C. N. 1999, A&AS, 140, 355
O'Dea, C. P., et al. 2006, ApJ, 653, 1115
Orienti, M., et al. 2010, A&A, submitted
Owen, F. N., & Laing, R. A. 1989, MNRAS, 238, 357
Piconcelli, E., et al. 2008, A&A, 480, 671
Rector, T. A., & Stocke, J. T. 2001, AJ, 122, 565
Smith, E. P., & Heckman, T. M. 1989, ApJS, 69, 365
Snowden, S., et al. 2004, The *XMM-Newton* ABC Guide (version 2.01)
Spergel, D. N., et al. 2007, ApJS, 170, 377
Spinrad, H., Marr, J., Aguilar, L., & Djorgovski, S. 1985, PASP, 97, 932
Struder, L., et al. 2001, A&A, 365, L18
Tadhunter, C., et al. 1993, MNRAS, 263, 999
Tadhunter, C., et al. 2002, MNRAS, 330, 977
Tadhunter, C., et al. 2007, ApJ, 661, 13
Tavecchio, F., et al. 2000, ApJ, 544, 23
Torresi, E., et al. 2009, A&A, 498, 61
Turner, M. L. J., et al. 2001, A&A, 365, L27
Van Breugel, W., Heckman, T., Butcher, H., & Miley, G. 1984, ApJ, 277, 82
Venturi, T., Morganti, R., Tzioumis, T., & Reynolds, J. 2000, A&A, 363, 84